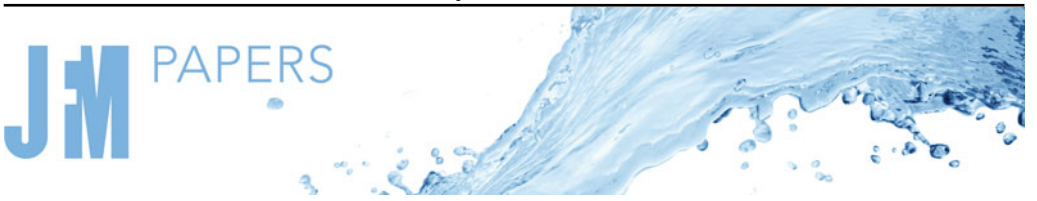
J. Fluid Mech. (2026), *vol.* 1036, A6, doi:10.1017/jfm.2026.11619



A theory for foam-driven fracturing

Zhong Zheng[1,2]

[1]State Key Laboratory of Ocean Engineering, School of Ocean and Civil Engineering, Shanghai Jiao Tong University, Shanghai 200240, PR China

[2]MOE Key Laboratory of Hydrodynamics, School of Ocean and Civil Engineering, Shanghai Jiao Tong University, Shanghai 200240, PR China

Corresponding author: Zhong Zheng, zzheng@alumni.princeton.edu; zhongzheng@sjtu.edu.cn

(Received 8 November 2025; revised 30 March 2026; accepted 29 April 2026)

We provide a theoretical model for foam-driven fracturing of an elastic solid. Based on recent experimental observations, we take into consideration the influence of foam rheology and compressibility. We arrive at a nonlinear non-local system that couples the dynamics of one-dimensional compressible plug flow of foam and elastic deformation of the infinite solid. The model leads to time-dependent solutions for the evolution of the fracture's profile shape and the pressure distribution in the film of foam. The solutions are affected by a dimensionless control parameter Π_c, which measures the influence of foam compressibility. An increase in Π_c leads to more significant expansion of the gas phase in the fracture, and the spreading of the film of foam is enhanced. Asymptotic efforts were also made in the weakly compressible regime. The profile now admits a linear asymptote $h \propto \chi$ as $\chi \equiv x_f - x \to 0^+$, compared with the standard viscous asymptote $h \propto \chi^{2/3}$ for hydraulic fracturing using incompressible Newtonian fluids. The pressure singularity now follows $p \propto \ln \chi$, which is weaker than the standard $p \propto \chi^{-1/3}$ singularity in the viscous regime. It is also observed that the profile shape and pressure distribution can be rescaled appropriately to collapse onto universal curves at intermediate times, with the length and pressure scales following the $x \propto t^{5/9}$, $h \propto t^{4/9}$ and $p \propto t^{-1/9}$ scaling laws. Using foam as the fracturing fluid may save water in practical applications such as enhanced gas recovery from shale rocks.

Key words: lubrication theory, thin films, elastic waves

1. Introduction

Hydraulic fracturing of elastic solids forms an interesting and important research topic (e.g. Spence & Sharp 1985; Lister 1990*a*; Savitski & Detournay 2002; Lai *et al.* 2015; OKeeffe, Huppert & Linden 2018*a*; Zheng 2025*a*), as it mimics some of the key fluid–structure interaction processes in geophysical, environmental and industrial applications.

© The Author(s), 2026. Published by Cambridge University Press.

https://doi.org/10.1017/jfm.2026.11619 Published online by Cambridge University Press

For example, this list includes the enhanced recovery of oil and gas (e.g. Bickle *et al.* 2012; Cueto-Felgueroso & Juanes 2013; Patzek, Male & Marder 2013), the formation of magma-driven dykes and lacolliths (e.g. Lister & Kerr 1991), and the motion of the grounding line that connects an ice sheet and an ice shelf (e.g. Warburton, Hewitt & Neufeld 2020). The application of this technology in the energy industry also draws environmental concerns, such as the generation of seismic waves (e.g. Schultz *et al.* 2018) and the migration of pollutants when the fracturing fluid flows back (e.g. Lai *et al.* 2016*b*; Zheng 2025*a*).

Previous studies have addressed the model problem of hydraulic fracturing of elastic solids in simple one-dimensional geometries using Newtonian fluids. The specific roles of fluid flow, elastic deformation and material breaking are clarified on the coupled evolution of the fracture's profile shape and the pressure distribution (e.g. Spence & Sharp 1985; Spence, Sharp & Turcotte 1987; Lister 1990*a*,*b*; Savitski & Detournay 2002; Detournay 2004; Zheng 2025*a*,*b*). Furthermore, laboratory experiments, typically performed in transparent elastic solids, provided useful insights by validating some of the most important theoretical predictions such as the frontal propagation laws and the universal profile shapes (e.g. Lai *et al.* 2015, 2016*a*,*b*, 2018; O'Keeffe & Linden 2017; O'Keeffe *et al.* 2018*a*,2018*b*; Tanikella & Dressaire 2022).

In the context of hydraulic fracturing for enhanced oil/gas recovery, it is well known that a large amount of water is consumed as the fracturing fluid. Also, the fracturing fluid could possibly pollute the drinking water layer when it flows back from rock formations once pressure is released (e.g. Lai *et al.* 2016*a*; Zheng 2025*a*). Alternative options include using foam (e.g. Lai *et al.* 2018) or gas (such as CO_2) (e.g. Wang *et al.* 2018) as the fracturing fluid, which possibly leads to a significant reduction of water consumption. Under typical working conditions, recent experiments show that foam compressibility and rheology could both affect the leading-order dynamics of fluid-driven fracturing (e.g. Lai *et al.* 2018), but theoretical development is yet to be provided.

The present work aims to provide a simple one-dimensional theory to describe the dynamics of foam-driven fracturing, building on some of the interesting experimental observations made by Lai *et al.* (2018). In particular, we take into consideration the influence of foam compressibility and rheology when we model the plug flow of foam. This leads to a modified Reynolds equation for the profile shape evolution of the film of foam. We also take into consideration the influence of foam flow in the injection conduit, which is integrated into the nonlinear non-local system as a flux boundary condition at the origin.

We note that the dynamics of hydraulic fracturing has also been studied when it is driven by the injection of non-Newtonian fluids. This is practically relevant because proppants or fibres are often added into a fracturing fluid, which modifies its rheological behaviours. For example, the influence of power-law fluid rheology has been reported on hydraulic fracturing of elastic solids (e.g. Lenoach 1995; Dontsov & Kresse 2018). The influence of Herschel–Bulkley fluid rheology has also been studied theoretically (e.g. Bessmertnykh & Dontsov 2019), which leads to plug flow patterns in the conduits and is also closely related to the present work on foam flow (e.g. Denkov *et al.* 2005, 2006; Lai *et al.* 2018).

This paper is structured as follows. In § 2, we first present a theoretical model for foam-driven fracturing, and a dimensionless control parameter Π_c is identified to measure the strength of foam compressibility. In § 3, we provide more insights into the weakly compressible and viscosity-dominated regime as $\Pi_c \to 0^+$ by studying the asymptotic behaviours in the tip region and the self-similar intermediate dynamics. Comparison with experimental observations is also attempted. The paper closes in § 4 with a brief summary and final remarks on potential implications.

https://doi.org/10.1017/jfm.2026.11619 Published online by Cambridge University Press

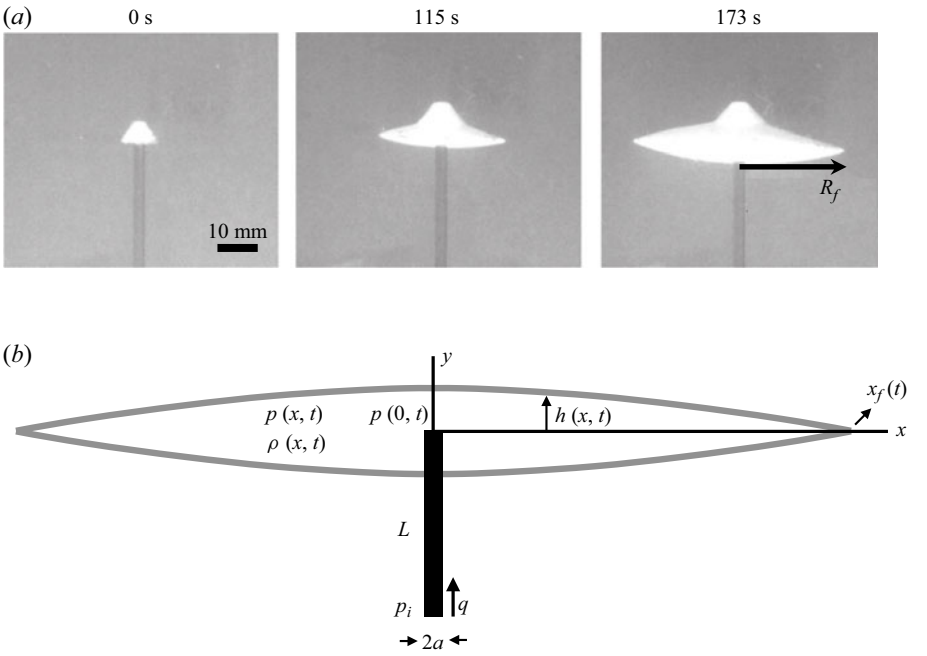


Figure 1. Foam-driven fracturing of an elastic solid. (*a*) Typical experimental observations of a foam-driven penny-shaped fracture in a solid gelatine (Lai *et al.* 2018). (*b*) Schematic of a foam-driven plain-strain fracture in the Cartesian configuration. The profile shape is denoted by $h(x, t)$, and the pressure and density distributions are denoted by $p(x, t)$ and $\rho(x, t)$, respectively. The length and half-width of the injection tube are denoted by L and a, respectively. The injection rate of the foam is denoted by $q(t)$, driven by the pressure difference between $p = p_i(t)$ at $y = 0$ (the inlet) and $p = p(0, t)$ at $y = L$ (the outlet) of the injection tube.

2. Theoretical model

We present a simple one-dimensional model to describe the dynamics of foam-driven fracturing of an infinite elastic solid. Compared with standard descriptions of hydraulic fracturing using incompressible Newtonian fluids such as water (e.g. Spence & Sharp 1985; Lister 1990*a*; Savitski & Detournay 2002), two additional effects are considered now that could become relevant at leading order, including the compressibility and the rheological effects of the foam flow. Here, we demonstrate the influence of foam compressibility and rheology in the context of planar fractures (i.e. plane-strain hydraulic fractures) in the Cartesian configuration. The radial configuration could also be studied in the same way for the development of penny-shaped foam-driven fractures. We consider only the viscosity-dominated regime in this work, and neglect any influence of material toughness.

2.1. *Governing equations*

We first take into consideration the compressibility effect of the foam flow. Denoting the profile shape as $h(x, t)$ for the film of foam, which is also the profile shape of the foam-driven fracture, the requirement of local continuity is written as

$$\frac{\partial}{\partial t}\left(\int_0^{h(x,t)} \rho(x, y, t)\,\mathrm{d}y\right) + \frac{\partial}{\partial x}\left(\int_0^{h(x,t)} \rho(x, y, t)\,u(x, y, t)\,\mathrm{d}y\right) = 0, \qquad (2.1)$$

https://doi.org/10.1017/jfm.2026.11619 Published online by Cambridge University Press

where $\rho(x, y, t)$ and $u(x, y, t)$ denote the density and the velocity fields, respectively. The profile shape $h(x, t)$ of a fracture is also termed the half 'fracture opening profile' or half 'fracture aperture profile' in the field or in the solid mechanics literature. It is also commonly denoted by $w(x, t)$. If we further neglect the influence of buoyancy, which is plausible in laboratory experiments since the film of foam is typically mm in thickness (e.g. Lai *et al.* 2018), then the density field reduces to $\rho(x, t)$ without the y dependence. Since foam flow typically evolves into a plug flow pattern with wall slip in one-dimensional tubes (e.g. Denkov *et al.* 2005, 2006; Lai *et al.* 2018), the velocity field also reduces to $u(x, t)$ without the y dependence. In this case, (2.1) further reduces to

$$\frac{\partial}{\partial t}\left[\rho(x, t)\, h(x, t)\right] + \frac{\partial}{\partial x}\left[\rho(x, t)\, u(x, t)\, h(x, t)\right] = 0. \tag{2.2}$$

Compared with the incompressible version of the local continuity equation, we now include in (2.2) an additional weighting function of the density of foam $\rho(x, t)$ in both the time and space derivatives. This form has been employed in a previous study of gas-driven fracturing (e.g. Wang *et al.* 2018).

The (net) pressure distribution due to elastic deformation is given by the standard integral expression

$$p(x, t) = -\frac{E}{2(1-\sigma^2)}\frac{1}{\pi}\int_0^{x_f(t)} \frac{2s}{s^2 - x^2}\frac{\partial h}{\partial s}\,\mathrm{d}s, \tag{2.3}$$

taking into account the contribution from both the negative and positive halves of the domain. Here, E is the Young's modulus of the elastic solid, and σ is the Poisson ratio (often denoted by ν in the solid mechanics literature). This remains the same as the standard description of hydraulic fracturing using Newtonian fluids (e.g. Spence & Sharp 1985). The integral expression (2.3) can be obtained by analysing the normal stress distribution at any specific location x, as induced by displacement continuities in the regime of linear elastostatics without the influence of body forces, followed by a superposition of the contribution of all of them throughout the entire domain (see e.g. the Appendix of Peirce 2025). We note again that $p(x, t)$ is the net pressure that is measured on the basis of any externally imposed far-field normal stress σ_∞ (e.g. Lister 1990*b*; Detournay 2004; Garagash 2006), and by definition the atmospheric pressure is already absorbed in σ_∞. Detailed discussions are also available in Garagash (2006) on the influence of σ_∞, which becomes negligibly small at sufficiently large times, and the transient time depends on its value.

For an ideal gas (such as air or CO_2), a linear law $\rho = p/(RT)$ typically applies between density and pressure, where T is temperature, and R is a gas constant. We consider only the isothermal system in this work. For foam, we employ the leading-order Taylor expansion next to a reference state of pressure p_0 and density ρ_0 as

$$\rho = \rho_0 + \left.\frac{\partial \rho}{\partial p}\right|_{p_0}(p - p_0) + \text{h.o.t.} \sim \rho_0 + c^{-2}(p - p_0), \tag{2.4}$$

where the speed of sound c is introduced. To be self-consistent, the pressures $p(x, t)$ and p_0 in (2.4) are also the net pressure on the basis of the far-field normal stress σ_∞. We expect that (2.4) provides a good estimate when the operation is around the reference pressure p_0, i.e. in the weakly compressible regime. Too far away from p_0, more appropriate nonlinear forms should be considered. Based on the form of (2.4), we see that the density $\rho(x, t)$ is dependent on the fracture's profile shape $h(x, t)$. A similar linear law has been employed recently to study the influence of flow compressibility on gas-driven fracturing (e.g. Wang *et al.* 2018).

https://doi.org/10.1017/jfm.2026.11619 Published online by Cambridge University Press

Parameter	Unit	Typical value	Physical description
μ	mPa s	29 ± 2	Liquid viscosity
γ	mN m^{-1}	3 ± 1	Interfacial tension
ϵ	–	0.1	Liquid volume fraction
κ	–	4.0	Resistance constant
r	μm	12 ± 1	Bubble radius
E	kPa	66	Young's modulus
σ	–	0.5	Poisson ratio
γ_s	J m^{-2}	1.0	Surface energy
K_c	Pa m$^{-1/2}$	363	Material toughness ($\sqrt{2E\gamma_s}$)
a	mm	1.08	Tube radius
L	m	0.43	Tube length
u	cm s^{-1}	1.5	Velocity of foam flow in a tube

Table 1. Typical parametric values for the fracturing process of a block of solid gelatine using a Gillette foam as the fracturing fluid in a laboratory experiment (e.g. Lai *et al.* 2018).

For foam flow in a straight tube, plug flow patterns would typically develop due to wall slip. The motion of the plug of foam is lubricated by a thin liquid film attaching to the wall. In the bulk region away from the wall, the foam would advance uniformly with a constant slip velocity u. The following result has been employed previously (e.g. Denkov *et al.* 2005, 2006; Lai *et al.* 2018) for the magnitude of the slip velocity:

$$|u| = \frac{r^2 a^2}{\gamma \mu \kappa^2} \left(\frac{\partial p}{\partial x}\right)^2, \tag{2.5}$$

where r is the (average) bubble size, a is the radius of the tube, μ is the viscosity of the liquid, γ is the interfacial tension, and $\kappa(\epsilon)$ is a (dimensionless) resistance constant that depends on the liquid volume fraction ϵ. For a sense of scales, typical values for the parameters are summarised in table 1 when fracturing a solid gelatine with Gillette foam as the fracturing fluid (Lai *et al.* 2018). There is also experimental evidence of (2.5); see e.g. figure 8 of Denkov *et al.* (2005), or figure 3 in the supplementary information of Lai *et al.* (2018). Compared with the laminar flow of incompressible Newtonian fluids in a tube where $|u| \propto \partial p/\partial x$, the plug flow of foam now follows $|u| \propto (\partial p/\partial x)^2$.

An important assumption of solution (2.5) is that the capillary number is sufficiently small (i.e. $Ca \equiv \mu\,|u|/\gamma \ll 1$) such that the wall shear stress follows $\tau_w/(\gamma/r) \propto Ca^{1/2}$. Based on the stress balance $\tau_w = -(a/2)(\partial p/\partial x)$, we then arrive at solution (2.5), introducing a resistance constant $\kappa(\epsilon)$. The transient dynamics towards this steady state (2.5) has also been neglected. We must note that the result $\tau_w \propto Ca^{1/2}$ for the wall shear stress is different from the classic result $\tau_w \propto Ca^{2/3}$ for standard viscous capillary films. The physical picture of the latter corresponds to a propagating Taylor bubble in straight tubes (e.g. Bretherton 1961). Brief comments are also provided in Appendix B regarding the leading-order physics behind the $\tau_w \propto Ca^{1/2}$ and $\tau_w \propto Ca^{2/3}$ behaviours for the wall shear stress.

To describe the film flow of foam inside a fracture of half-thickness $h(x, t)$, we modify (2.5) by replacing the radius a of the tube by $h(x, t)$, which leads to

$$|u(x, t)| = \frac{r^2 h(x, t)^2}{\gamma \mu \hat{\kappa}} \left(\frac{\partial p}{\partial x}\right)^2 \tag{2.6}$$

https://doi.org/10.1017/jfm.2026.11619 Published online by Cambridge University Press

for the magnitude of the slip velocity. The two major physical components remain the same: The wall shear stress follows $\tau_w/(\gamma/r) \propto Ca^{1/2}$ for the plug flow of foam, and the stress balance follows $\tau_w = -(h/2)(\partial p/\partial x)$ in the confined space of half-opening $h(x,t)$. Since $h(x,t)$ is now allowed to vary slowly with t and x, for the latter we have also made the assumption of lubrication approximation. We also recognise the difference in configuration between (2.5) (for tube flow) and (2.6) (for planar flow), so we expect appropriate corrections being provided by a different resistance constant $\hat{\kappa}(\epsilon)$. We also neglect the influence of clogging/jamming for viscoplastic flow in converging conduits (e.g. Rallabandi *et al.* 2017). To understand more about the theory of viscoplastic thin film flows and the appearance of pseudo-yield surfaces, an interested reader can also refer to e.g. Balmforth & Craster (1999) and Taylor-West & Hogg (2021) for more recent developments.

We then arrive at a coupled evolution system for the profile shape $h(x,t)$ of a foam-driven fracture and the pressure field $p(x,t)$ within the foam film, and at leading order this is given by

$$\frac{\partial}{\partial t}\big(\big[\rho_0 + c^{-2}(p-p_0)\big]h\big) - \frac{r^2}{\gamma\mu\hat{\kappa}^2}\frac{\partial}{\partial x}\left[\big[\rho_0 + c^{-2}(p-p_0)\big]\,h^3\left(\frac{\partial p}{\partial x}\right)^2\right] = 0, \quad (2.7a)$$

$$p(x,t) = -\frac{E}{2(1-\sigma^2)}\frac{1}{\pi}\int_0^{x_f(t)} \frac{2s}{s^2-x^2}\frac{\partial h}{\partial s}\,\mathrm{d}s. \quad (2.7b)$$

Compared with hydraulic fracturing with incompressible Newtonian fluids (e.g. Spence & Sharp 1985), the Reynolds equation (2.7*a*) has been modified accordingly to absorb the influence of foam compressibility based on (2.4) and foam rheology based on (2.6). Equation (2.7*b*) for the elastic pressure remains unchanged.

The governing system (2.7*a*,*b*) is ready to be solved, providing the following appropriate initial and boundary conditions (IBC):

$$h(x,0) = 0, \quad p(x,0) = 0, \quad (2.8a)$$

$$h(x_f,t) = 0, \quad (2.8b)$$

$$\frac{r^2}{\gamma\mu\kappa^2}\big[\rho_0 + c^{-2}(p-p_0)\big]h^3\left(\frac{\partial p}{\partial x}\right)^2\bigg|_{x=0} = q(t), \quad (2.8c)$$

where $q(t)$ is the mass rate of the foam flow that enters the first quadrant of the domain (per unit depth perpendicular to the plane of paper). Physically, the initial condition (2.8*a*) indicates that there is no fracturing fluid within the elastic solid before fracturing occurs, and the net pressure is zero. Equation (2.8*b*) is a frontal condition, which corresponds to the location of the fracture's tip. Equation (2.8*c*) is a flux condition, which describes how fast fluid accumulates inside the fracture. It is also assumed that the half-width a of the injection tube is much smaller than the half-length $x_f(t)$ of the fracture, such that the tube can be treated as located at approximately $x = 0$. To determine the influx $q(t)$, we next consider the plug flow of the foam inside the straight tube, through which foam is delivered into the elastic solid to create a fracture.

2.2. *Determining the influx $q(t)$*

The compressible plug flow of foam in the injection tube is driven by the pressure difference $\Delta p \equiv p_i(t) - p(0,t)$ between the inlet ($y = 0$) and outlet ($y = L$) of the tube. Here, $p_i(t)$ denotes the net pressure imposed at the inlet of the injection tube, while $p(0,t)$ denotes the net pressure at the centre of the fracture (which is also the outlet of the injection tube). Based on (2.5), we obtain $q(t) = \rho u a/2$ into the first quadrant without

https://doi.org/10.1017/jfm.2026.11619 Published online by Cambridge University Press

considering any transient dynamics, and this is a quarter of the total flux $2\rho ua$ into the fracture. Furthermore, we obtain

$$q(t) = \frac{r^2 a^3}{2\gamma\mu\hat{\kappa}^2}\left[\rho_0 + c^{-2}(p - p_0)\right]\left(\frac{\partial p}{\partial y}\right)^2, \tag{2.9}$$

the right-hand-side of which must be y-independent for any quasi-steady operations.

Solution (2.9) can be further rearranged to provide the (nonlinear) pressure distribution along the tube:

$$p(y,t) = \left[p_i(t)^{3/2} - \left(\frac{9\gamma\mu\hat{\kappa}^2 c^2\, q(t)}{2r^2a^3}\right)^{1/2} y\right]^{2/3} - \left(\rho_0 c^2 - p_0\right). \tag{2.10}$$

The influx $q(t)$ can then be determined:

$$q(t) = \frac{9r^2a^3c^4}{8\gamma\mu\hat{\kappa}^2L^2}\left(\left[\rho_0 + c^{-2}(p_i(t) - p_0)\right]^{3/2} - \left[\rho_0 + c^{-2}(p(0,t) - p_0)\right]^{3/2}\right)^2, \tag{2.11}$$

which applies when $\Delta p \equiv p_i(t) - p(0,t) \geqslant 0$.

It is easily seen that (2.10) and (2.11) are both different from the corresponding results when the fracturing fluid is an incompressible Newtonian fluid, in which case $p(y,t)$ depends linearly on y (e.g. Zheng 2025*a*,*b*). Another useful insight from solution (2.11) is that to enforce a constant injection rate q into the fracture, the inlet pressure $p_i(t)$ must adjust accordingly with the outlet pressure $p(0,t)$, the value of which must be determined by solving the full nonlinear non-local evolution system. In this work, we consider only the constant-pressure operations when the inlet pressure p_i is an imposed constant.

2.3. *Non-dimensionalisation*

We have now formulated a complete problem of foam-driven fracturing with a set of governing equations (2.7*a*,*b*) for the coupled evolution of the profile shape $h(x,t)$ and pressure field $p(x,t)$. Equations (2.7*a*,*b*) are to be solved subject to appropriate IBC (2.8*a*–*c*). The influx $q(t)$ in (2.8*c*) is given further by (2.11). The evolution is driven by an externally imposed inlet pressure $p_i(t)$ at the entrance of the injection tube, and in this work, p_i is an imposed constant. The density of foam is denoted as ρ_i at this (net) pressure. In the equation of state (2.4), we now impose $(p_0, \rho_0) = (p_i, \rho_i)$ as the reference (net) pressure and density, which allows us to obtain the density values subject to foam compression/expansion.

It is standard first to non-dimensionalise the model problem before solving it analytically or numerically. The dimensionless variables are defined as $\bar{t} \equiv t/t_c$, $\bar{\rho} \equiv \rho/\rho_c$, $\bar{p} \equiv p/p_c$, $\bar{x} \equiv x/x_c$ and $\bar{h} \equiv h/h_c$, and the characteristic scales are chosen as

$$t_c = \frac{9E^5\gamma\mu\hat{\kappa}^2\rho_i^2c^4a^3}{256\pi^5(1-\sigma^2)^5r^2L^2p_i^9}, \quad \rho_c = \rho_i, \;\; p_c = p_i, \tag{2.12a}$$

$$x_c = \frac{9E^3\rho_i^2c^4a^3}{64\pi^3(1-\sigma^2)^3L^2p_i^5}, \quad h_c = \frac{9E^2\rho_i^2c^4a^3}{32\pi^2(1-\sigma^2)^2L^2p_i^4}. \tag{2.12b}$$

The characteristic pressure and density scales are chosen as (p_i, ρ_i) based on the injection condition. The characteristic time, length and thickness scales are chosen based on the Reynolds equation for the foam flow, the elastic equation for pressure, and the influx boundary condition for foam accumulation, such that the coefficients become 1 in their dimensionless form. Physically, this suggests that at dimensionless time $\bar{t} = 1$, all physical

https://doi.org/10.1017/jfm.2026.11619 Published online by Cambridge University Press

effects come into play at leading order, including both the complex flow and the elastic deformation.

We then arrive at the dimensionless system

$$\frac{\partial}{\partial \bar{t}}\left[(1+\Pi_c(\bar{p}-1))\bar{h}\right]-\frac{\partial}{\partial \bar{x}}\left[(1+\Pi_c(\bar{p}-1))\bar{h}^3\left(\frac{\partial \bar{p}}{\partial \bar{x}}\right)^2\right]=0, \tag{2.13a}$$

$$\bar{p}=-\int_0^{\bar{x}_f(\bar{t})}\frac{2s}{s^2-\bar{x}^2}\frac{\partial \bar{h}}{\partial s}\,\mathrm{d}s, \tag{2.13b}$$

subject to dimensionless IBC

$$\bar{h}(\bar{x},0)=0,\quad \bar{p}(\bar{x},0)=0, \tag{2.14a}$$

$$\bar{h}(\bar{x}_f,\bar{t})=0, \tag{2.14b}$$

$$(1+\Pi_c(\bar{p}-1))\bar{h}^3\left(\frac{\partial \bar{p}}{\partial \bar{x}}\right)^2\Big|_{\bar{x}=0}=\left(1-[1+\Pi_c(\bar{p}(0,\bar{t})-1)]^{3/2}\right)^2. \tag{2.14c}$$

We are then ready to solve (2.13*a*,*b*) subject to IBC (2.14*a*-*c*) for the dynamics of foam-driven fracturing under constant pressure operations.

We have also identified a dimensionless parameter

$$\Pi_c\equiv\frac{p_i}{\rho_i c^2}. \tag{2.15}$$

Physically, $\Pi_c^{1/2}$ is the Mach number at speed $(p_i/\rho_i)^{1/2}$, hence Π_c measures the compressibility of the plug flow of foam. We only consider the subsonic regime $\Pi_c\in(0,1)$ of foam compression/expansion in the present work. A greater Π_c corresponds to more significant compressible effects in both the injection tube and the fracture, while $\Pi_c\to 0^+$ corresponds to the incompressible limit. The value of Π_c distinguishes the 'compressible' and 'incompressible' regimes of foam-driven fracturing.

We can also focus on the fracture itself and evaluate its global mass/volume evolution:

$$\bar{M}(\bar{t})\equiv\int_0^{\bar{x}_f(\bar{t})}[1+\Pi_c(\bar{p}-1)]\bar{h}(\bar{x},\bar{t})\,\mathrm{d}\bar{x},\quad \bar{V}(\bar{t})\equiv\int_0^{\bar{x}_f(\bar{t})}\bar{h}(\bar{x},\bar{t})\,\mathrm{d}\bar{x}, \tag{2.16}$$

where $\bar{M}(\bar{t})$ is the dimensionless mass of the foam inside a fracture, while $\bar{V}(\bar{t})$ is the dimensionless volume. Their evolution depends on many physical aspects of the model problem, including the plug flow of the foam, compressibility of the foam flow, elastic deformation of the infinite solid, and the dynamic coupling of all of them.

2.4. *Numerical observations*

We first make some representative calculations with different values of Π_c to illustrate the different dynamics of foam-driven fracturing, as shown in figures 2 and 3. Key insights obtained are as follows.

(i) Influence of foam compressibility. It is observed in the numerical simulations that the fluid pressure decreases from the origin towards the fracture's tip location, and so as the density of the foam (due to the expansion of the gas phase). An increase in Π_c leads to more serious decrease of the fluid pressure and the foam density. Correspondingly, this leads to a more significant increase in fluid volume, and hence a more significant enhancement of film spreading and fracture propagation, as shown

https://doi.org/10.1017/jfm.2026.11619 Published online by Cambridge University Press

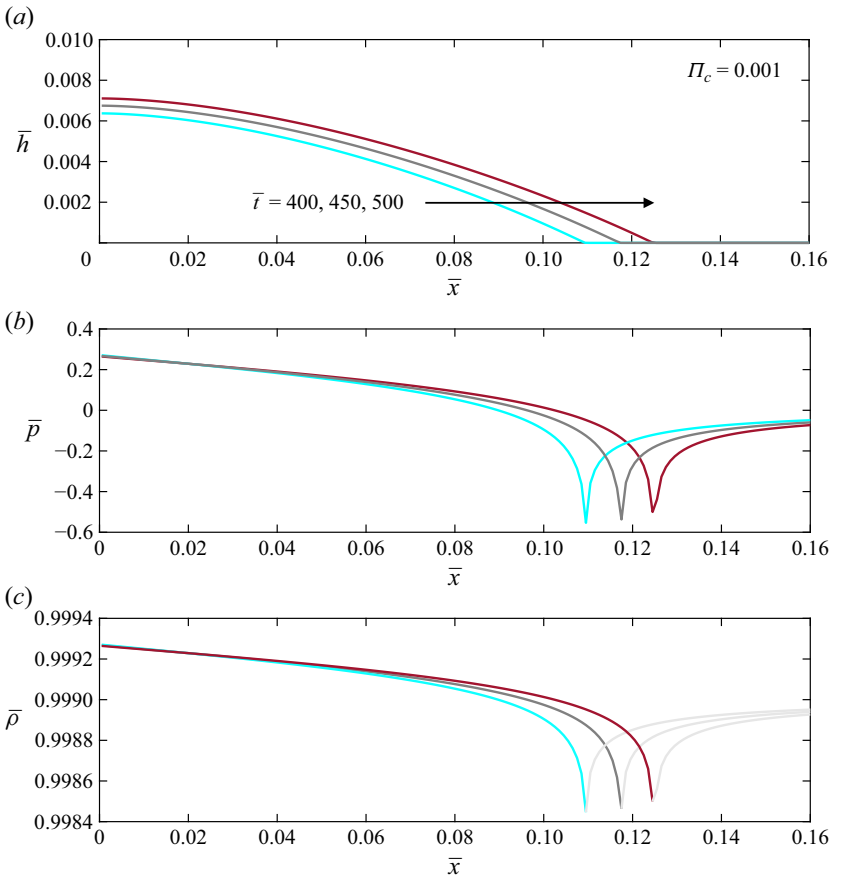


Figure 2. Representative numerical solutions of foam-driven fracturing at dimensionless times $\bar{t} = 400, 450, 500$, when we impose $\Pi_c = 0.001$. The $\bar{p}(\bar{x}, \bar{t})$ values ahead of the front represent the normal elastic stress along the axis, while the $\bar{\rho}(\bar{x}, \bar{t})$ values ahead of the front contain no physical meaning because there exists no fluid. We have imposed $N = 200$ space grids on a domain with $\bar{L}_d = 0.2$ in this simulation; see § A.1. In the bulk region there is reasonable convergence, even though in a narrow region close to the fracture's tip, the pressure singularity is still under the influence of grid refinement. The density solutions ahead of the fracture's tip have no physical meaning and are marked with a different colour.

in figures 2 and 3. Furthermore, the volume accumulation departs from the linear law in time due to foam expansion, as shown in figure 4, and the departure becomes more significant as Π_c increases.

(ii) Influence of foam rheology. The plug flow nature of the foam flow leads to modified profile shapes and pressure distributions, compared with standard results of hydraulic fracturing using incompressible Newtonian fluids (e.g. Spence & Sharp 1985). In particular, we have observed a linear asymptotic shape towards the fracture's tip in the weakly compressible regime in the numerical simulations, as shown in figures 2 and 3. This is to be contrasted with the well-known $h \propto (x_f - x)^{2/3}$ viscous asymptote when the fracturing fluid is Newtonian. Later, we prove that the tip asymptotes follow $h \propto (x_f - x)$ and $p \propto \log(x_f - x)$ as $x \to x_f^-(t)$ as $\Pi_c \to 0^+$ in the weakly compressible regime.

https://doi.org/10.1017/jfm.2026.11619 Published online by Cambridge University Press

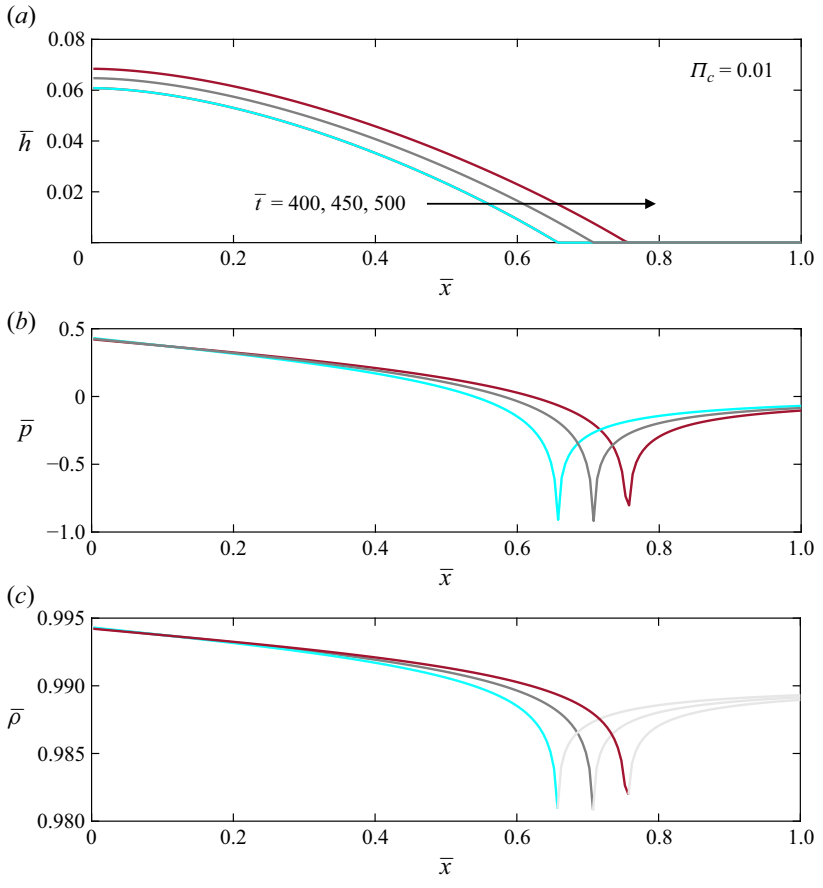


Figure 3. Representative numerical solutions of foam-driven fracturing at dimensionless times $\bar{t} =$ 400, 450, 500, when we impose $\Pi_c = 0.01$. We have imposed $N = 200$ space grids on a domain with $\bar{L}_d = 1.0$ in this simulation; see § A.1. In the bulk region, there is reasonable convergence, even though in a narrow region close to the fracture's tip, the pressure singularity is still under the influence of grid refinement. The density solutions ahead of the fracture's tip have no physical meaning and are marked with a different colour.

3. Analytical insights into the weakly compressible regime

One important feature of foam-driven fracturing is the distinction of the compressible and incompressible regimes. Specifically, the dimensionless density of the working fluid is given by

$$\bar{\rho}(\bar{x}, \bar{t}) = 1 + \Pi_c(\bar{p}(\bar{x}, \bar{t}) - 1), \tag{3.1}$$

which enters the problem in the Reynolds equation (2.13*a*). It also enters the description (2.11) for foam flow in the injection tube, and hence the influx condition (2.14) that describes how foam accumulates in the fracture. The compressibility of the foam flow is controlled by the value of Π_c. Note also that $\bar{\rho} > 0$ must always be ensured.

When $\Pi_c \ll 1$, we approach the weakly compressible regime of foam-driven fracturing, and we are able to make some analytical progress in this asymptotic limit for more insights.

https://doi.org/10.1017/jfm.2026.11619 Published online by Cambridge University Press

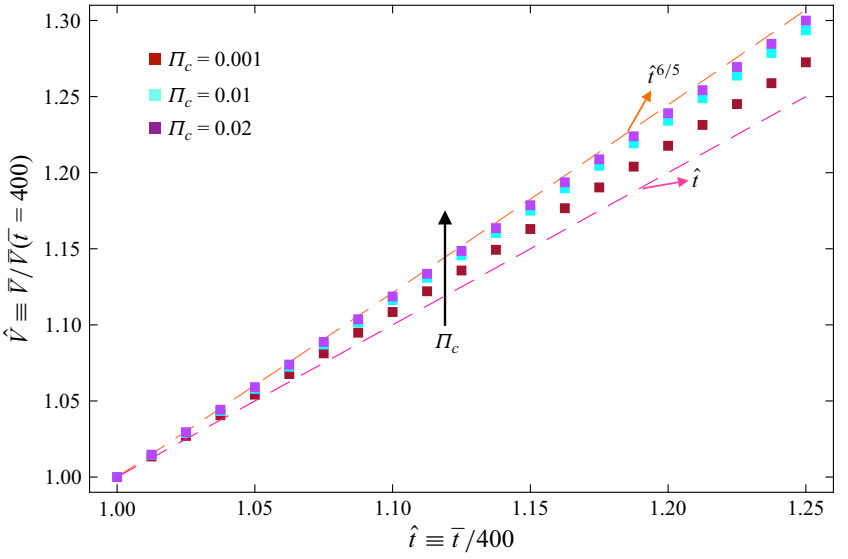


Figure 4. The influence of Π_c (which measures foam compressibility) on the time evolution of the total volume $\bar{V}(\bar{t})$ of a foam-driven fracture. Here, we include the appropriately rescaled numerical data of the fracture's volume for the period $\bar{t} \in [400, 500]$ for three values of Π_c (i.e. $\Pi_c = 0.001, 0.01, 0.02$). The solutions $\hat{V} = \hat{t}$ and $\hat{V} = \hat{t}^{6/5}$ are also included for comparison: an increase in Π_c leads to more significant influence of foam compressibility, as it departs more significantly from the linear accumulation law. Specifically, power-law fitting of these numerical data provides $\hat{V} \sim 1.00\,\hat{t}^{1.08}$ when $\Pi_c = 0.001$, $\hat{V} \sim 1.00\,\hat{t}^{1.15}$ when $\Pi_c = 0.01$, and $\hat{V} \sim 1.00\,\hat{t}^{1.18}$ when $\Pi_c = 0.02$. The R^2 values are 1.00 for all three fittings.

Specifically, the governing equations (2.13*a*,*b*) reduce to

$$\frac{\partial \bar{h}}{\partial \bar{t}} - \frac{\partial}{\partial \bar{x}}\left[\bar{h}^3 \left(\frac{\partial \bar{p}}{\partial \bar{x}}\right)^2\right] = 0, \tag{3.2a}$$

$$\bar{p} = -\int_0^{\bar{x}_f(\bar{t})} \frac{2s}{s^2 - \bar{x}^2} \frac{\partial \bar{h}}{\partial s}\, \mathrm{d}s \tag{3.2b}$$

at leading order, which are to be solved subject to the IBC (2.14). Furthermore, the flux condition (2.14*c*) reduces to

$$\bar{h}^3 \left(\frac{\partial \bar{p}}{\partial \bar{x}}\right)^2 \bigg|_{\bar{x}=0} \sim \frac{9}{4}\Pi_c^2 \left[\bar{p}(0, \bar{t}) - 1\right]^2 \tag{3.3}$$

at leading order, which highlights the role of Π_c. It is clearly seen that due to the influence of foam rheology, the Reynolds equation (3.2*a*) is still different from the standard form of hydraulic fracturing using Newtonian fluids (e.g. Spence & Sharp 1985).

3.1. *Asymptotic structure near the tip of the fracture*

It is of use to have some insights on the asymptotic structure near the fracture's tip for both the profile shape $\bar{h}(\bar{x}, \bar{t})$ and the pressure distribution $\bar{p}(\bar{x}, \bar{t})$. Unfortunately, there seems to be no self-similar behaviour for all time, since the injection rate (3.3) depends on $(\bar{p}(0, \bar{t}) - 1)^2$. However, the tip shape can still be studied based on the assumption of quasi-steady evolution (e.g. Lister, Peng & Neufeld 2013; Hewitt, Balmforth & Bruyn

https://doi.org/10.1017/jfm.2026.11619 Published online by Cambridge University Press

2015), which must be verified, however, based on appropriate comparisons with numerical solutions of the full time-dependent problem.

We define $\chi \equiv \bar{x}_f(\bar{t}) - \bar{x}$ as the distance from the tip location $\bar{x}_f(\bar{t})$, and we now evaluate $\bar{h}(\chi)$ and $\bar{p}(\chi)$ as $\chi \to 0^+$ at any specific time $\bar{t}$ of interest. Equations (3.2*a*,*b*) further reduce to

$$c\bar{h} - \bar{h}^3 \left(\frac{\mathrm{d}\bar{p}}{\mathrm{d}\chi}\right)^2 = 0, \tag{3.4a}$$

$$\bar{p} = -\int_0^\infty \frac{2s}{s^2 - \chi^2} \frac{\mathrm{d}\bar{h}}{\mathrm{d}s}\, \mathrm{d}s, \tag{3.4b}$$

where $c \equiv \mathrm{d}\bar{x}_f/\mathrm{d}\bar{t}$ is the speed of advancement of the fracture's tip.

We now impose the power-law form of the profile shape near the tip,

$$\bar{h}(\chi) \sim A\chi^\alpha, \tag{3.5}$$

as $\chi \to 0^+$, and the integral (3.4*b*) for elastic pressure leads to (e.g. Spence & Sharp 1985; Peirce 2025)

$$\bar{p}(\chi) \sim \begin{cases} A\alpha \cot(\pi\alpha)\, \chi^{\alpha-1}, & \alpha \in (1/2,\, 1), \\ A\pi^{-1} \log \chi, & \alpha = 1. \end{cases} \tag{3.6}$$

Substituting (3.5) and (3.6) into the Reynolds equation (3.4*a*), now considering only the influence of plug flow of foam in the weakly compressible limit, the correct balance leads to $\alpha = 1$. Hence we must admit

$$\bar{h}(\chi) \sim A\chi, \quad \bar{p}(\chi) \sim A\pi^{-1} \log \chi, \tag{3.7}$$

where $A = c^{1/4}\pi^{1/2}$.

This $\bar{h}(\chi) \propto \chi$ tip asymptote in the viscosity-dominated regime is fundamentally different from the well-known $\bar{h}(\chi) \propto \chi^{2/3}$ tip asymptote of hydraulic fracturing using incompressible Newtonian fluids (e.g. Spence & Sharp 1985; Detournay 2004). This asymptote is also different from the $\bar{h}(\chi) \propto \chi^{1/2}$ tip asymptote in the material toughness-dominated regime. Its appearance is not due to foam compressibility, but due to the plug flow nature of foam rheology (2.6). The result (3.7) is verified based on a comparison with the numerical solutions of the full time-dependent problem, as shown in figure 5, normalised by the maximum fracture opening in each case. We show the range $\chi \in [0.1,\, 1]$ here for $\Pi_c = 0.001,\, 0.01$, where the numerical solutions are more accurate (sufficiently far away from the tip region with pressure singularity, which requires more space grids to clearly capture numerically).

It may be of interest to note that this linear asymptotic profile $\bar{h}(\chi) \propto \chi$ has also been obtained in a recent study on hydraulic fracturing using Herschel–Bulkley fluids (Bessmertnykh & Dontsov 2019), by setting $n = 0$ in the imposed viscoplastic constitutive law $\tau = \tau_0 + k\dot{\gamma}^n$ for perfectly plastic fluids. Note also that the model is formulated in a moving coordinate system along with the fracture's tip, which is different from the present work (except in § 3.1 for the tip asymptotes), which maintains the time evolution in the Reynolds equation. Furthermore, the linear asymptotic profile $\bar{h}(\chi) \propto \chi$ is also achievable using an incompressible power-law fluid ($\tau = k\dot{\gamma}^m$) for hydraulic fracturing, imposing $m = 0$ (e.g. Dontsov & Kresse 2018).

Furthermore, $\bar{p}(\chi) \propto \log \chi$ is weaker than $\bar{p}(\chi) \propto \chi^{-1/3}$ for tip asymptotes in the viscosity-dominated regime of hydraulic fracturing with Newtonian fluids. It is also weaker than the $\bar{p}(\chi) \propto \chi^{-1/2}$ tip asymptote in the toughness-dominated regime. The tip asymptote for pressure is more difficult to capture numerically due to the existence of the

https://doi.org/10.1017/jfm.2026.11619 Published online by Cambridge University Press

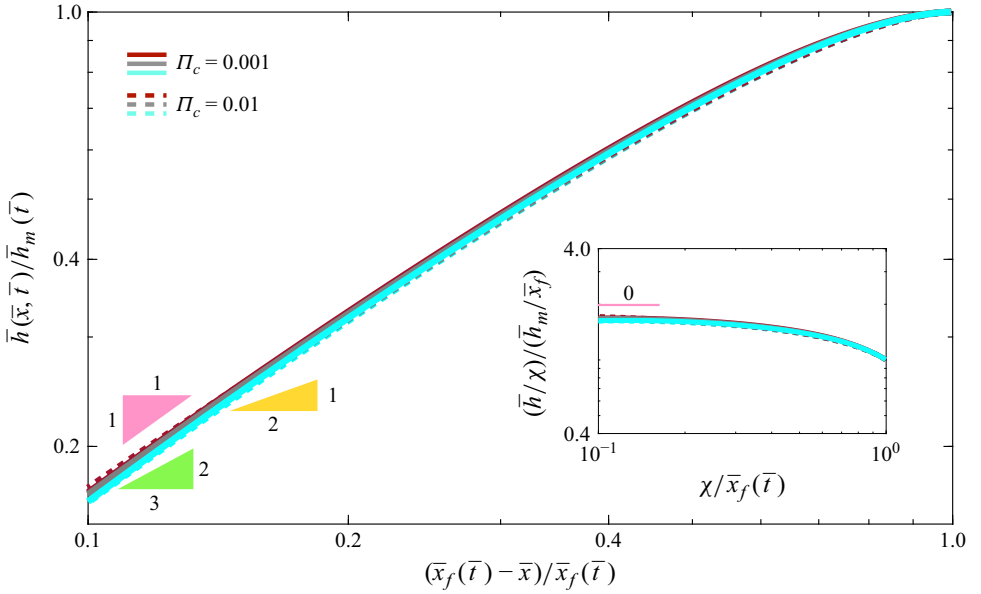


Figure 5. The profile shape, normalised by its maximum value, near the fracture's tip in the weakly compressible regime (as $\Pi_c \to 0^+$) from the numerical solutions of the full time-dependent problem. Numerical data are taken from figure 2(*a*) for $\Pi_c = 0.001$ and figure 3(*a*) for $\Pi_c = 0.01$. The theoretical prediction (3.7) (slope 1) is also included for comparison. The slopes 1/2 (toughness-dominated regime) and 2/3 (viscosity-dominated regime) are also included, as the standard results of hydraulic fracturing using incompressible Newtonian fluids. The inset indicates that $\bar{h}/\chi$ indeed approaches a constant moving close to the tip region.

pressure singularity, which is well known. With some $N = 200$ space grids imposed in the present work, we found that the $\bar{p}(\chi) \propto \log \chi$ singularity is not clearly captured in the numerical solutions.

3.2. *Self-similar evolution when $\bar{p}(0,\bar{t})$ remains approximately constant*

Because the injection rate (3.3) depends on $(\bar{p}(0,\bar{t})-1)^2$, there seems to be no self-similar structure throughout the entire period of time evolution. However, if pressure $\bar{p}(0,\bar{t})$ remains approximately unchanged during some finite time period of interest, then we expect the evolution to follow approximately a self-similar fashion in the viscosity-dominated regime.

Standard scaling analysis of (3.2*a*,*b*) and (3.3), under the assumption that $\bar{p}(0,\bar{t})$ is constant, indicates that

$$\frac{\bar{x}}{\bar{t}} \propto \frac{\bar{h}^3\bar{p}^2}{\bar{x}^3}, \quad \bar{p} \propto \frac{\bar{h}}{\bar{x}}, \quad \bar{h}\bar{x} \propto \bar{t}, \tag{3.8}$$

and after some rearrangement, we arrive at

$$\bar{x} \propto \bar{t}^{5/9}, \quad \bar{h} \propto \bar{t}^{4/9}, \quad \bar{p} \propto \bar{t}^{-1/9}, \tag{3.9}$$

which shows that pressure $\bar{p}(\bar{x},\bar{t})$ evolves really with time. However, the evolution is quite slow and follows a $\bar{t}^{-1/9}$ time dependence, which suggests that the assumption that $\bar{p}(0,\bar{t})$ remains approximately unchanged could be a reasonable assumption for quite a period of time. For example, when the time evolution covers one order of magnitude, the pressure scale becomes $10^{-1/9} \approx 0.77$ times the initial value. When the time evolution

https://doi.org/10.1017/jfm.2026.11619 Published online by Cambridge University Press

covers two orders of magnitude, the pressure scale becomes $100^{-1/9} \approx 0.60$ times the initial value. When the time evolution covers three orders of magnitude, the pressure scale becomes $1000^{-1/9} \approx 0.46$ times the initial value. All these calculations suggest that the assumption of neglecting the time evolution of pressure $\bar{p}(0, \bar{t})$ could be a reasonable one for time periods that cover up to several orders of magnitude. This is verified based on the numerical solutions of the full time-dependent system, as we show later.

We next define a similarity variable as $\xi \equiv \bar{x}/\bar{t}^{5/9}$, and explore self-similar solutions for the evolution of the profile shape $\bar{h}(\bar{x}, \bar{t})$ and pressure field $\bar{p}(\bar{x}, \bar{t})$ in the forms $\bar{h}(\bar{x}, \bar{t}) = \bar{t}^{4/9}\, \mathcal{K}(\xi)$ and $\bar{p}(\bar{x}, \bar{t}) = \bar{t}^{-1/9}\, \mathcal{G}(\xi)$, respectively. We obtain

$$\frac{4}{9}\mathcal{K} - \frac{5}{9}\xi \frac{\mathrm{d}\mathcal{K}}{\mathrm{d}\xi} - \frac{\mathrm{d}}{\mathrm{d}\xi}\left[\mathcal{K}^3 \left(\frac{\mathrm{d}\mathcal{G}}{\mathrm{d}\xi}\right)^2\right] = 0, \tag{3.10a}$$

$$\mathcal{G}(\xi) = -\int_0^{\xi_f} \frac{2s}{s^2 - \xi^2} \frac{\mathrm{d}\mathcal{K}}{\mathrm{d}s}\, \mathrm{d}s, \tag{3.10b}$$

where $\xi_f \equiv \bar{x}_f(\bar{t})/\bar{t}^{5/9}$ is the frontal location. The ordinary differential system (3.10*a*,*b*) is solved subject to boundary conditions

$$-\mathcal{K}^3 \left(\frac{\mathrm{d}\mathcal{G}}{\mathrm{d}\xi}\right)^2 \bigg|_{\xi=0} = \frac{9}{4}\Pi_c^2 \left[\bar{p}(0, \bar{t}) - 1\right]^2, \tag{3.11a}$$

$$\mathcal{K}(\xi_f) = 0. \tag{3.11b}$$

Now the inlet pressure $\bar{p}(0, \bar{t})$ is an imposed constant without any time evolution. This is an approximation, but it could be quite a reasonable one when the time evolution spans up to several orders of magnitude.

The self-similar system (3.10*a*,*b*) can be solved numerically with (3.11) using the same numerical scheme that we have used in several previous studies (e.g. Zheng 2024, 2025*a*,*b*). The central idea is to maintain the time dependence in the similarity transform, defining $\tau \equiv -\ln \bar{t}$ and $\xi \equiv \bar{x}/\bar{t}^{5/9}$, and transform the original system (3.2*a*,*b*) in the $(\bar{x}, \bar{t})$ space into the (τ, ξ) space. We then numerically solve the system in the (τ, ξ) space until there is no time evolution, and the steady-state solution provides the self-similar solution of interest. Brief remarks are also provided in § A.3.

We then provide a comparison in figure 6 between the normalised numerical solutions $\bar{h}(\bar{x}, \bar{t})$ and $\bar{p}(\bar{x}, \bar{t})$ of the partial differential integral system (2.13*a*,*b*) and the self-similar solutions $\mathcal{K}(\xi)$ and $\mathcal{G}(\xi)$ of the ordinary differential integral system (3.10*a*,*b*), when the pressure $\bar{p}(0, \bar{t})$ remains approximately constant. Here, we have imposed $\Pi_c = 0.001$ in the weakly compressible and viscosity-dominated regime. The numerical solutions of (3.2*a*,*b*) are provided at $\bar{t} = 400, 450, 500$, and $\bar{p}(0, \bar{t}) = 0.27$ is taken as its initial value at $\bar{t} = 400$ in (3.11*a*). We have observed reasonably good agreement between the normalised time-dependent solutions and the self-similar solutions in this regime. For comparison, the well-known self-similar solutions of hydraulic fracturing using incompressible Newtonian fluids are included also as the square symbols in the same figure (e.g. Spence & Sharp 1985; Detournay 2004).

Furthermore, the corresponding frontal laws are shown in figure 7, imposing $\Pi_c = 0.001$, along with a comparison with the theoretical prediction (3.9) in the viscosity-dominated and weakly compressible regime of foam-driven fracturing. We have also observed fairly good agreement between the theoretical and numerical results.

https://doi.org/10.1017/jfm.2026.11619 Published online by Cambridge University Press

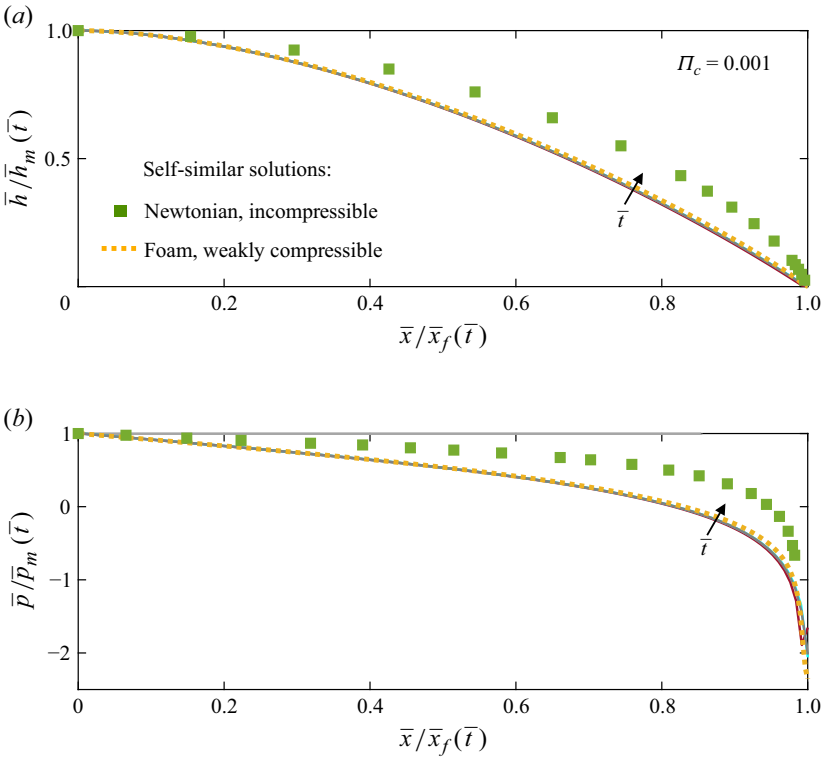


Figure 6. Comparison between the normalised numerical solutions $\bar{h}(\bar{x}, \bar{t})$ and $\bar{p}(\bar{x}, \bar{t})$ of the original time-dependent system (2.13*a*,*b*), and the self-similar solutions $\mathcal{K}(\xi)$ and $\mathcal{G}(\xi)$ from solving (3.10*a*,*b*). The numerical solutions are the appropriated rescaled ones in figure 2 at $\bar{t} = 400$, 450, 500 when $\Pi_c = 0.001$. The self-similar solutions from solving (3.10*a*,*b*) are included as the dashed curves for comparison. The self-similar solutions of hydraulic fracturing using incompressible Newtonian fluids are included also as square symbols (e.g. Spence & Sharp 1985; Detournay 2004). In the flux condition (3.11*a*), the pressure at the origin is imposed as a constant $\bar{p}(0, \bar{t}) = 0.270$ for this time period based on the numerical data in figure 7(*d*).

3.3. *Remarks on the experimental observations of Lai et al. (2018)*

One useful note is that the tip asymptote (3.7) as obtained in the Cartesian configuration should also apply in the radial configuration. Hence it could be used to be compared with experimental observations of penny-shaped foam-driven fractures as well. As an example, we deal with the final-time profile shape at $t = 173$ s in the experiment in figure 1, as performed by Lai *et al.* (2018). We then obtain a comparison with solution (3.7) in the $(\chi, h/h_m)$ space for the fracture's profile shape in the tip region in figure 8. Arguably, there is a reasonable degree of agreement between the theoretical prediction and the experimental observation. But the agreement is not as good as that in figure 5.

Meanwhile, it is observed in the experiments of Lai *et al.* (2018) that the time evolution of the fracture's volume could significantly depart from the $V \propto t$ linear law, using foam as the fracturing fluid. This was attributed to the influence of foam compressibility. This is consistent with the numerical observations in figure 4, even though foam is now injected under constant-pressure operations, which is different from how it is supplied in the experiments of Lai *et al.* (2018). Furthermore, we observe that an increase in the value of Π_c leads to more significant departure from the linear accumulation law. All these observations illustrate the influence of foam compressibility.

https://doi.org/10.1017/jfm.2026.11619 Published online by Cambridge University Press

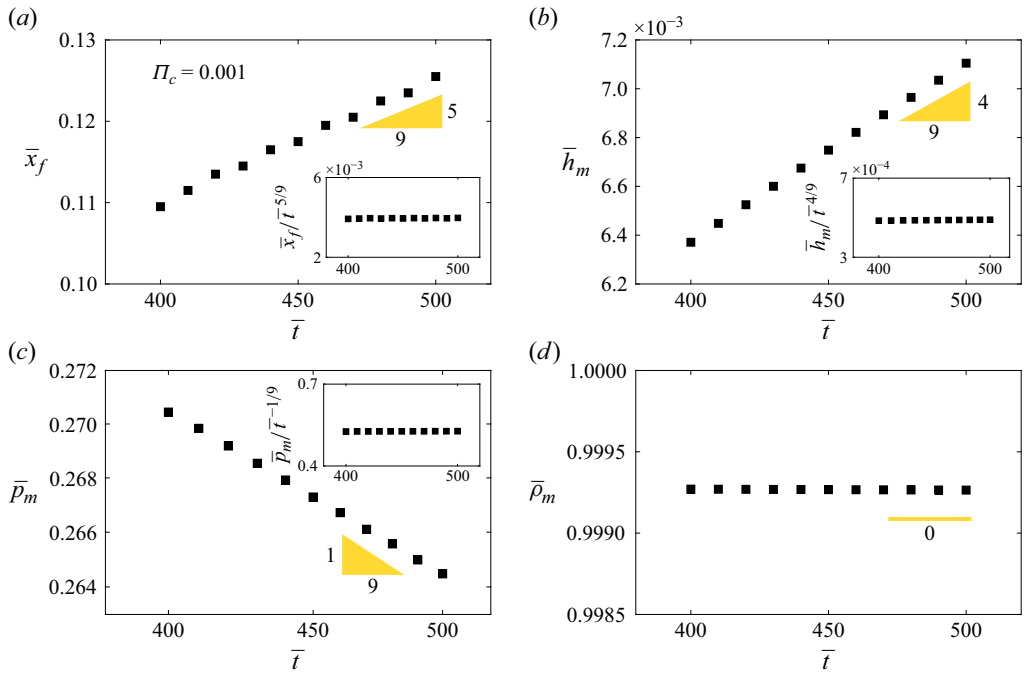


Figure 7. The propagation laws in the weakly compressible and viscosity-dominated regime of foam-driven fracturing. Here, we have provided numerical solutions of the frontal location $\bar{x}_f(\bar{t})$, inlet thickness $\bar{h}_m(\bar{t}) = \bar{h}(0, \bar{t})$, maximum pressure $\bar{p}_m(\bar{t}) = \bar{p}(0, \bar{t})$, and maximum density $\bar{\rho}_m(\bar{t}) = \bar{\rho}(0, \bar{t})$. The numerical solutions are obtained by solving the original system (2.13*a*,*b*) for the period $\bar{t} \in [400, 500]$ when $\Pi_c = 0.001$. The scaling results (3.9*a*–*c*) are also included for comparison. The insets of (*a*–*c*) show that the appropriately rescaled values by their corresponding power-law time dependences become time-independent.

It may also be of use to comment on one more interesting observation: when we stretch the self-similar solutions in figure 6 for the profile shape in both the x and h directions, we are able to obtain very promising agreement with the experimentally measured profiles, as shown in figure 9. This seems to suggest that for this experiment, the profile shape of a foam-driven fracture is predominantly affected by the specific foam rheology. Indeed, we have imposed the plug flow rheology in the model based on the experimental measurement of Lai *et al.* (2018). The profile shape depends only weakly on the radial geometry and other experimental features such as how the foam is supplied.

4. Summary and final remarks

4.1. *Brief summary*

We have investigated the dynamics of foam-driven fracturing of an infinite elastic solid. Compared with the standard models of hydraulic fracturing using incompressible Newtonian fluids, we now take into consideration the influence of foam compressibility and foam rheology. We arrived at a modified Reynolds equation that describes the dynamics of foam-driven fracturing, which is coupled with the standard integral equation for elastic pressure. The influence of the plug flow of foam in the injection tube is integrated appropriately as a flux boundary condition.

https://doi.org/10.1017/jfm.2026.11619 Published online by Cambridge University Press

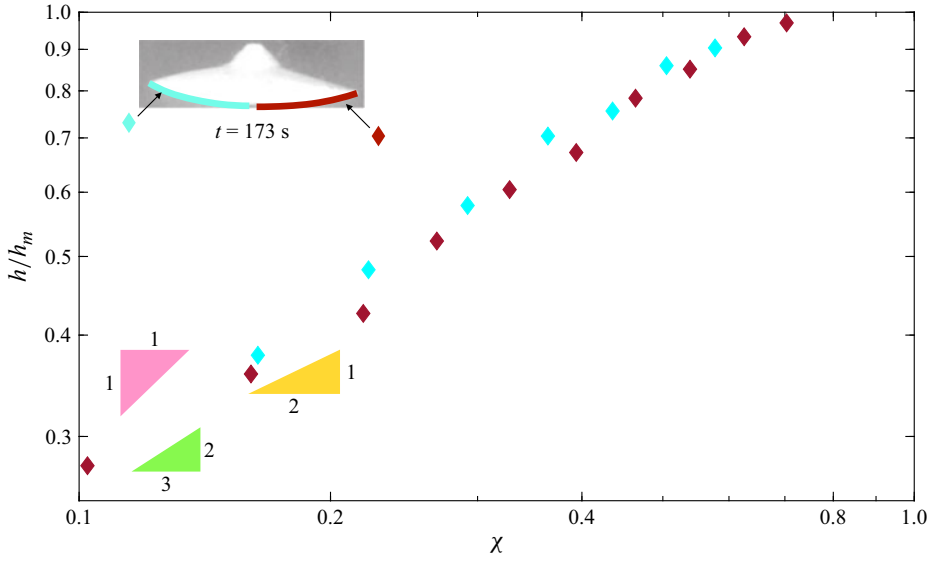


Figure 8. The profile shape near the fracture's tip at the final time ($t = 173$ s) of the experiment shown in figure 1, as performed by Lai *et al.* (2018). The theoretical prediction (3.7) (slope 1) is also included for a comparison, now with $\chi \equiv (R_f - R)/R_f$, where $R_f(t)$ denotes the frontal location of the penny-shaped fracture. The slopes $1/2$ (toughness-dominated regime) and $2/3$ (viscosity-dominated regime) are also included, as the standard results of hydraulic fracturing using incompressible Newtonian fluids.

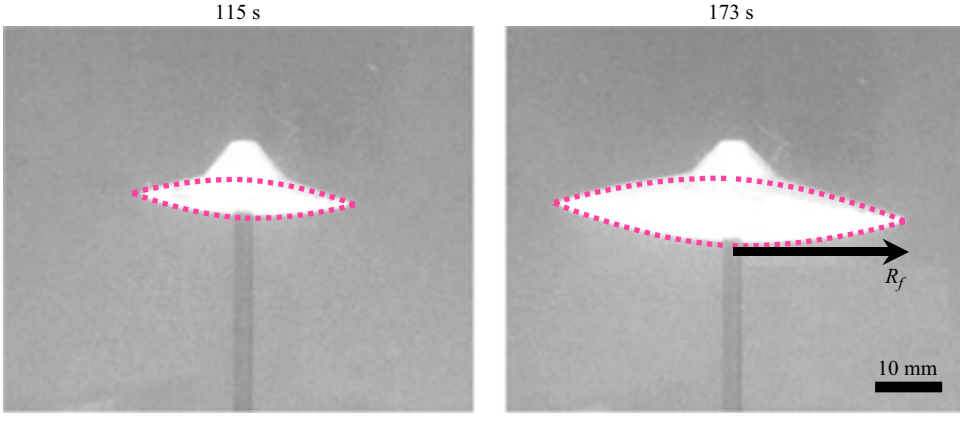


Figure 9. The profile shapes in the experiment of Lai *et al.* (2018), along with a comparison with the numerical solutions in the viscosity-dominated and weakly compressible regime. Here, the theoretical profile shape is taken from the universal shape in figure 6 and stretched in both the x and h directions for the best match with the experimental profiles.

Upon appropriate non-dimensionalisation, a dimensionless control parameter Π_c has been identified, which affects the dynamics of foam-driven fracturing. Physically, Π_c measures the relative influence of compressibility, and its value distinguishes the compressible and incompressible regimes. The dynamics of foam-driven fracturing are then demonstrated through numerical solutions of the nonlinear non-local system. Asymptotic analysis has also been attempted to obtain more insights into the weakly compressible regime.

Regarding the influence of the foam compressibility, because fluid pressure always decreases from the origin towards the tip location of a fracture, introducing compressibility

https://doi.org/10.1017/jfm.2026.11619 Published online by Cambridge University Press

always leads to an expansion of the gas phase and hence a decrease in the density of the foam. This feature enhances the spreading of the foam film and the propagation of the foam-driven fracture. Time evolution of the fracture's total volume departs also from the linear accumulation law due to gas expansion, and this departure becomes more significant as Π_c increases.

Regarding the influence of the foam rheology, we obtain a linear asymptotic profile shape $h \propto \chi$ as $\chi \to 0^+$ in the weakly compressible regime, which is to be compared with the well-known $h \propto \chi^{2/3}$ asymptote for hydraulic fracturing with incompressible Newtonian fluids. This asymptote has been verified based on a comparison with the time-dependent numerical solutions. This asymptote is also, arguably, consistent with the experimental observations made by Lai *et al.* (2018), even though the fracture is penny-shaped in the experiments. Meanwhile, the pressure singularity becomes weaker as $p \propto \log \chi$, to be compared with the standard result $p \propto \chi^{-1/3}$.

We have also observed that the inlet pressure $p(0, t)$ remains approximately constant in the weakly compressible regime during the time evolution for up to several decades. This indicates that the inlet flux of foam into the fracture remains constant. Correspondingly, there exist $x \propto t^{5/9}$, $h \propto t^{4/9}$ and $p \propto t^{-1/9}$ (which is indeed very slow) scaling laws for the evolution of the length and pressure scales. The fracture's profile shape and pressure distribution can also be rescaled to collapse onto universal solutions during the target period of time evolution.

We note also that we have neglected the influence of material toughness K_c in this work, which typically requires integrating an additional crack propagation condition into the model problem (e.g. Lister 1990*b*; Savitski & Detournay 2002; Zheng 2025*a*). For hydraulic fracturing using Newtonian fluids, a fracture could evolve into an elliptic shape and propagate in a quasi-steady fashion, when the influence of material toughness is dominant. For foam-driven fracturing, its influence remains to be explored. Brief remarks are included in Appendix C.

4.2. *Potential implications*

Hydraulic fracturing has been known to consume a large amount of water in the context of energy resource recovery. Using foam as an alternative fracturing fluid has the potential to significantly reduce the consumption of water. In the future, it would be of interest to study foam-driven fracturing, e.g. in the context of shale gas recovery. This requires appropriate inputs of the foam rheology and compressibility at reservoir conditions. It would also be of interest to study the backflow dynamics following foam-driven fracturing, which is related to the risk of drinking water pollution.

Before we close this paper, we provide brief comments regarding the influence of foam compressibility at reservoir conditions. To fracture a typical shale rock of Young's modulus $E = 15$ GPa, when a typical fracture of length $x_f = 1.0$ km and thickness $h_m = 10$ mm is generated, the elastic stress due to crack opening is estimated to be $p_f = Eh_m/x_f \approx 0.15$ MPa. Presuming that the shale formation locates at some 1–3 km underneath the ground surface, a reasonable estimate of the external normal stress σ_∞ (due to gravity) would be $\mathcal{O}(10)$ MPa. That said, the density change of foam along a fracture, which is related to the pressure change, is likely very small (say, 1 %, neglecting the pressure singularity in tip region). Hence the present model, imposing a linear law between ρ and p under the assumption of small pressure variations, is likely practically relevant for quantitative insights, and so are the example calculations in the weakly compressible regime. Also, the real impact of using foam as the fracturing fluid in the field is likely regarding its rheology (at high pressure and temperature, probably).

https://doi.org/10.1017/jfm.2026.11619 Published online by Cambridge University Press

But the major influence of foam compressibility likely occurs during its flow in the injection well before a fracture is initiated, to our understanding. Its influence is also likely non-negligible during a short initial period of fast expansion right after a fracture is generated. These arguments are also based on typical experimental observations of foam/gas-driven fracturing in solid gelatines. The underlying physics, within the framework of linear elastic fracture mechanics, is that for a fracture to initiate, the stress intensity factor (which is $\propto p$) must be large enough to overcome the influence of material toughness K_c (i.e. to break the atomic/molecular bonds), a typical value of which is $\mathcal{O}(10^2)$ Pa m$^{1/2}$ for a solid gelatine, and $\mathcal{O}(1)$ MPa m$^{1/2}$ for a shale rock. More discussions are included in Appendix C regarding the initial period of foam compression in the injection well, along with the influence of material toughness.

Funding. We acknowledge partial support from a QJMAM award (no. 1017777) and an Eastern Scholar Distinguished Professorship (no. TP2020009).

Declaration of interests. The authors report no conflict of interest.

Appendix A. Numerical schemes

A.1. Numerical scheme for the time-dependent system

We briefly describe a finite volume scheme that is employed to solve for the coupled evolution of the fracture's profile shape and the pressure distribution within the fluid film during the injection of foam. Specifically, we now deal with (2.13*a*,*b*) subject to (2.14) for constant pressure operations. Similar schemes have been employed in a series of our previous studies on the dynamics of hydraulic fracturing in a Hele-Shaw cell (Zheng 2024) and fluid withdrawal from hydraulic fractures in an elastic solid through a narrow conduit (e.g. Zheng 2025*a*,*b*). Similar schemes have also been employed to solve the gravity current injection problems into a thin layer of porous rock when the pressure distribution depends locally on the profile shape (e.g. Zheng *et al.* 2015; Hinton & Woods 2018; Zheng & Neufeld 2019). Finite volume schemes can also be employed to study hydraulic fracturing problems in the two-dimensional configuration (e.g. Peirce & Detournay 2008; Dontsov & Peirce 2017).

The evolution (2.13*a*) is first rewritten as

$$\frac{\partial m}{\partial t} - \frac{\partial q}{\partial x} = 0, \tag{A1}$$

where we have defined two auxiliary functions of mass $m(x, t)$ and flux $q(x, t)$ in the forms

$$m \equiv (1 + \Pi_c(p-1))h, \quad q \equiv (1 + \Pi_c(p-1))h^3 \left(\frac{\partial p}{\partial x}\right)^2. \tag{A2}$$

We focus on the dimensionless model here, but we no longer keep the bars for simplicity.

We start by discretising the domain of total length L_d into N equally spaced cells, each of which has the same length $\Delta x = L_d/N$, and the grids are allocated at the centres of the cells for the implementation of the finite volume scheme. Specifically, the grids locate at $x_n = (n - 1/2)\,\Delta x$, with $n = 1, 2, 3, \ldots, N$. The discretised values for the profile shape and pressure are denoted by h_n^i and p_n^i, respectively, with $i = 1, 2, 3, \ldots, I$ denoting the time steps, and by definition $t = (i-1)\,\Delta t$. The time step is chosen by $\Delta t = \hat{c}\,\Delta x^3$ based on the CFL condition, with $\hat{c}$ denoting a constant that is small enough to ensure that the scheme is stable. We also make use of the flux functions $q_{n+1/2}^i$, and they are defined at the boundary between two neighbouring grids.

https://doi.org/10.1017/jfm.2026.11619 Published online by Cambridge University Press

The discretised form of the evolution equation (A1) is

$$m_n^{i+1} = m_n^i + \frac{\Delta t}{\Delta x}\left(q_{n+1/2}^i - q_{n-1/2}^i\right) \tag{A3}$$

for any space grids ($n = 1, 2, 3, \ldots, N$) and at any time steps ($i = 1, 2, 3, \ldots, I$). The discretised form of (A2) at time step i is given by

$$m_n^i = \left[1 + \Pi_c\left(p_n^i - 1\right)\right] h_n^i \tag{A4}$$

for any space grid $n = 1, 2, \ldots, N$, and

$$q_{n+1/2}^i = \left[1 + \Pi_c\left(\frac{p_{n+1}^i + p_n^i}{2} - 1\right)\right]\left(\frac{h_{n+1}^i + h_n^i}{2}\right)^3 \left(\frac{p_{n+1}^i - p_n^i}{\Delta x}\right)^2 \tag{A5}$$

for the bulk region of $n = 2, \ldots, N-1$. At the two ends of the domain, we impose the flux boundary conditions

$$q_{1/2}^i = \left[1 - \left(1 + \Pi_c\left(p_1^i - 1\right)\right)^{3/2}\right]^2, \quad q_{N+1/2}^i = 0. \tag{A6}$$

Finally, at any time step $i = 1, 2, 3, \ldots, I$, the pressure equation (2.13*b*) of linear elasticity is discretised in the same way as in our previous studies (e.g. Zheng 2025*a*,*b*):

$$p_n^i = -\left[\sum_{k=1}^{n_f} \frac{h_{k+1}^i - h_k^i}{(x_{k+1} + x_k)/2 - x_n} + \sum_{k=1}^{n_f} \frac{h_{k+1}^i - h_k^i}{(x_{k+1} + x_k)/2 + x_n}\right], \tag{A7}$$

where n_f denotes the frontal location of the fracture.

We have now obtained a finite volume scheme that can be employed to solve for the coupled evolution of the profile shape $h(x, t)$ and pressure field $p(x, t)$ for foam-driven fracturing, imposing constant inlet pressures at the entrance of the inlet tube. Provided with a set of initial conditions $h_n^1 = 0$ and $p_n^1 = 0$, we are able to obtain the numerical solutions for m_n^i and p_n^i at any following time step $i = 2, 3, 4, \ldots, I$, hence $h_n^i = m_n^i/[1 + \Pi_c (p_n^i - 1)]$, by definition. The space step Δx is chosen to be small enough such that no significant difference is observed upon further grid refinement, as measured by e.g. the difference in the tip location in different simulation runs with different resolutions. The scheme is explicit in time and second-order in space. A typical number that we imposed in this work is approximately $N = 200$, and the solution curves shown in this work typically cover more than 100 space grids. Again, the treatment is consistent with our previous studies on hydraulic fracturing with Newtonian fluids. We also observe that the scheme is more stable for smaller Π_c values.

A.2. Numerical treatment for the self-similar system

To obtain the self-similar solutions of (3.10*a*,*b*) subject to (3.11), we now keep the time dependence in the similarity transform by introducing $\tau = \ln \bar{t}$, $\xi \equiv \bar{x}/\bar{t}^{5/9}$, $\bar{h}(\bar{x}, \bar{t}) = \bar{t}^{4/9} K(\xi)$ and $\bar{p}(\bar{x}, \bar{t}) = \bar{t}^{-1/9} G(\xi)$. The original time-dependent system (2.13*a*,*b*) is then transformed into

$$-\frac{\partial K}{\partial \tau} + \frac{4}{9}K - \frac{5}{9}\xi \frac{\partial K}{\partial \xi} = \frac{\partial}{\partial \xi}\left[K^3 \left(\frac{\partial G}{\partial \xi}\right)^2\right], \tag{A8a}$$

$$G(\xi) = -\int_0^{\xi_f} \frac{2s}{s^2 - \xi^2} \frac{\partial K}{\partial s}\, \mathrm{d}s, \tag{A8b}$$

https://doi.org/10.1017/jfm.2026.11619 Published online by Cambridge University Press

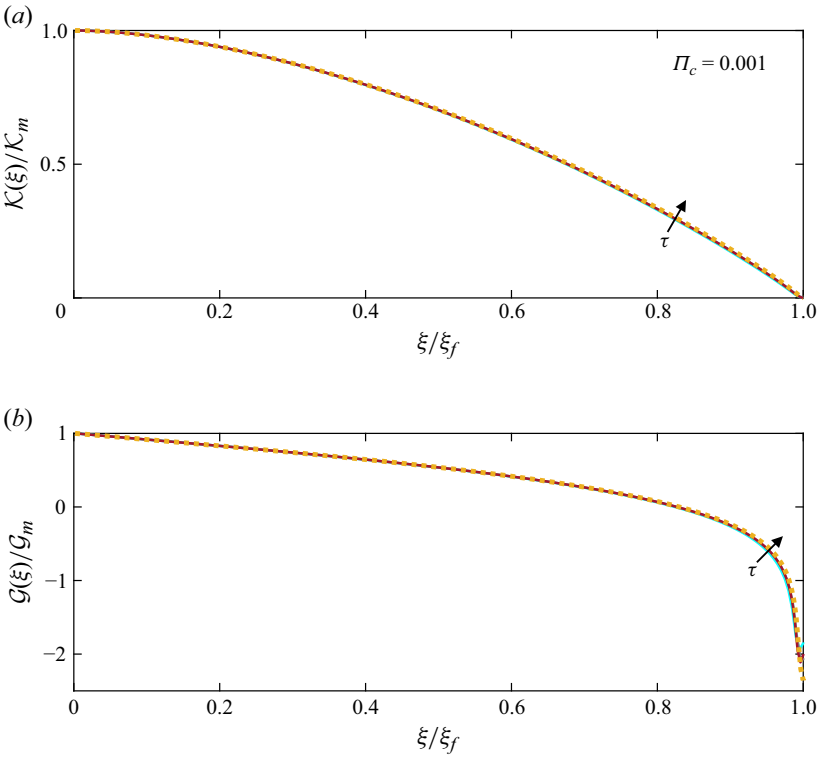


Figure 10. Calculation of (*a*) the universal profile shape $\mathcal{K}(\xi)/\mathcal{K}_m$ and (*b*) the pressure distribution $\mathcal{G}(\xi)/\mathcal{G}_m$ when $\Pi_c = 0.001$. Here, we impose $\bar{p}(0, \bar{t}) = 0.270$ in the flux condition (A9*b*) based on the numerical observations in figure 7(*d*), and we then solve (A8*a*,*b*) until $\tau = 5.25$. The solutions are shown at $\tau = 4.50, 4.75, 5.00, 5.25$, and the solutions at the final time $\tau = 5.25$ are what we include in figure 6 for a comparison, shown as the dashed curves. We have imposed $N = 800$ space grids on a domain of length $L_d = 0.2$.

to be solved subject to

$$K(0, \xi) = 0, \tag{A9a}$$

$$-K^3 \left(\frac{\partial G}{\partial \xi}\right)^2 \bigg|_{\xi=0} = \frac{9}{4}\Pi_c^2 \left[\bar{p}(0, \bar{t}) - 1\right]^2, \quad K(\tau, \xi_f) = 0. \tag{A9b}$$

Here, $\bar{p}(0, \bar{t})$ is imposed as a constant, as noted before. We use a finite volume scheme very similar to that described in § A.1 to solve (A8). We observe that for a sufficiently long period of time, there is no longer any significant evolution for the rescaled solutions, as shown in figure 10. The steady-state numerical solutions then become the self-similar solutions $\mathcal{K}(\xi)/\mathcal{K}_m$ and $\mathcal{G}(\xi)/\mathcal{G}_m$ that we are looking for, i.e.

$$K(\tau, \xi)/K_m(\tau) \to \mathcal{K}(\xi)/\mathcal{K}_m, \quad G(\tau, \xi)/G_m(\tau) \to \mathcal{G}(\xi)/\mathcal{G}_m, \tag{A10a}$$

as $\tau \to \infty$. This method has been employed in some of our previous studies on hydraulic fracturing using Newtonian fluids (e.g. Zheng 2024, 2025*a*,*b*).

A.3. Comparison between numerical and series solutions

To obtain more insights into the convergence of the code, we now compare with numerical solutions with available series solutions in previous reports. Instead of having such a comparison for foam-driven fracturing with compressible and rheological effects, we

https://doi.org/10.1017/jfm.2026.11619 Published online by Cambridge University Press

provide a comparison for the standard case of hydraulic fracturing using incompressible Newtonian liquids under constant injection rates and without leakage, in which case there are well-tested self-similar solutions in terms of series solutions (e.g. Spence & Sharp 1985; Detournay 2004). There is a similar comparison in figure 14 in the Appendix of Zheng (2025*a*), with a focus on the normalised solutions.

The appropriately rescaled governing system for this standard situation is given by (e.g. Spence & Sharp 1985; Detournay 2004; Zheng 2025*a*)

$$\frac{\partial \bar{h}}{\partial \bar{t}} - \frac{\partial}{\partial \bar{x}}\left(\bar{h}^3 \frac{\partial \bar{p}}{\partial \bar{x}}\right) = 0, \tag{A11a}$$

$$\bar{p} = -\int_0^{\bar{x}_f(\bar{t})} \frac{2s}{s^2 - \bar{x}^2} \frac{\partial \bar{h}}{\partial s}\, \mathrm{d}s, \tag{A11b}$$

which is also nonlinear non-local and is to be solved subject to dimensionless IBC

$$\bar{h}(\bar{x}, 0) = 0, \quad \bar{h}(\bar{x}_f(\bar{t}), \bar{t}) = 0, \quad -\bar{h}^3 \frac{\partial \bar{p}}{\partial \bar{x}}\bigg|_{\bar{x}=0} = 1, \tag{A12}$$

along with a tip propagation condition

$$\frac{\bar{h}}{(\bar{x}_f - \bar{x})^{1/2}} = \Pi_k \quad \text{as } \bar{x} \to \bar{x}_f(\bar{t})^-. \tag{A13}$$

The dimensionless toughness in (A13) is defined as $\Pi_k \equiv K_c[32(1-\sigma^2)^3/(3\pi\mu q E^3)]^{1/4}$. Very similar numerical schemes (see e.g. Appendices of Zheng 2025*a*,*b*) have been employed to solve the governing system for the time evolutions of $\bar{h}(\bar{x}, \bar{t})$ and $\bar{p}(\bar{x}, \bar{t})$. The numerical solutions obtained can be compared with the series solutions (e.g. Spence & Sharp 1985; Detournay 2004) in the self-similar regime to obtain insights into how the scheme works.

We first test the viscosity-dominated regime without the influence of material toughness, and the comparison is shown in figures 11(*a*) and 12(*a*). In particular, we show numerical solutions at three different times, $\bar{t} = 0.8, 0.9, 1.0$. Here, we have imposed $N = 300$ space grids on a domain of length $L_d = 1.5$ in the numerical simulation. The original profile and pressure solutions are also normalised to enforce a valid comparison, and the corresponding self-similar solutions for the profile shape (Spence & Sharp 1985) and pressure field (Detournay 2004) are included as the symbols. It is seen that the overall agreement is already reasonable at this grid resolution. Approaching the pressure singularity at the location of the fracture's tip, some disagreement starts to appear for the pressure solutions, which is as expected. Furthermore, based on the series solutions reported previously (e.g. Spence & Sharp 1985; Detournay 2004), the frontal laws are $\bar{x}_f \sim 1.33\,\bar{t}^{2/3}$, $\bar{h}_m \sim 1.08\,\bar{t}^{1/3}$ and $\bar{p}_m \sim 2.95\,\bar{t}^{-1/3}$, included also in figure 12(*a*) as the dashed lines, assuming that self-similarity is achieved and time transition is finished. Based on the numerical scheme to calculate the self-similar solutions reported recently (e.g. Zheng 2025*a*,*b*), the frontal laws are $\bar{x}_f \sim 1.35\,\bar{t}^{2/3}$, $\bar{h}_m \sim 1.04\,\bar{t}^{1/3}$ and $\bar{p}_m \sim 2.92\,\bar{t}^{-1/3}$, using some 200 space grids. The difference between the frontal laws for the two methods is already small, and is likely to further decrease by increasing the grid resolution.

We then test the toughness-dominated regime as $\Pi_k \to \infty$, when a fracture takes always an elliptic shape $(\bar{x}/\bar{x}_f)^2 + (\bar{h}/\bar{h}_m)^2 = 1$ and evolves quasi-steadily as injection proceeds, satisfying the propagation condition $\bar{h}/(\bar{x}_f - \bar{x})^{1/2} = \Pi_k$ as $\bar{x} \to \bar{x}_f$. It is easy to obtain the frontal laws $\bar{x}_f \sim 2^{5/3}\pi^{-2/3}\Pi_k^{-2/3}\,\bar{t}^{2/3}$ and $\bar{h}_m \sim 2^{1/3}\pi^{-1/3}\Pi_k^{2/3}\,\bar{t}^{1/3}$, which also satisfies $\pi \bar{x}_f \bar{h}_m = 4\bar{t}$ to conserve mass. Furthermore, based on the propagation

https://doi.org/10.1017/jfm.2026.11619 Published online by Cambridge University Press

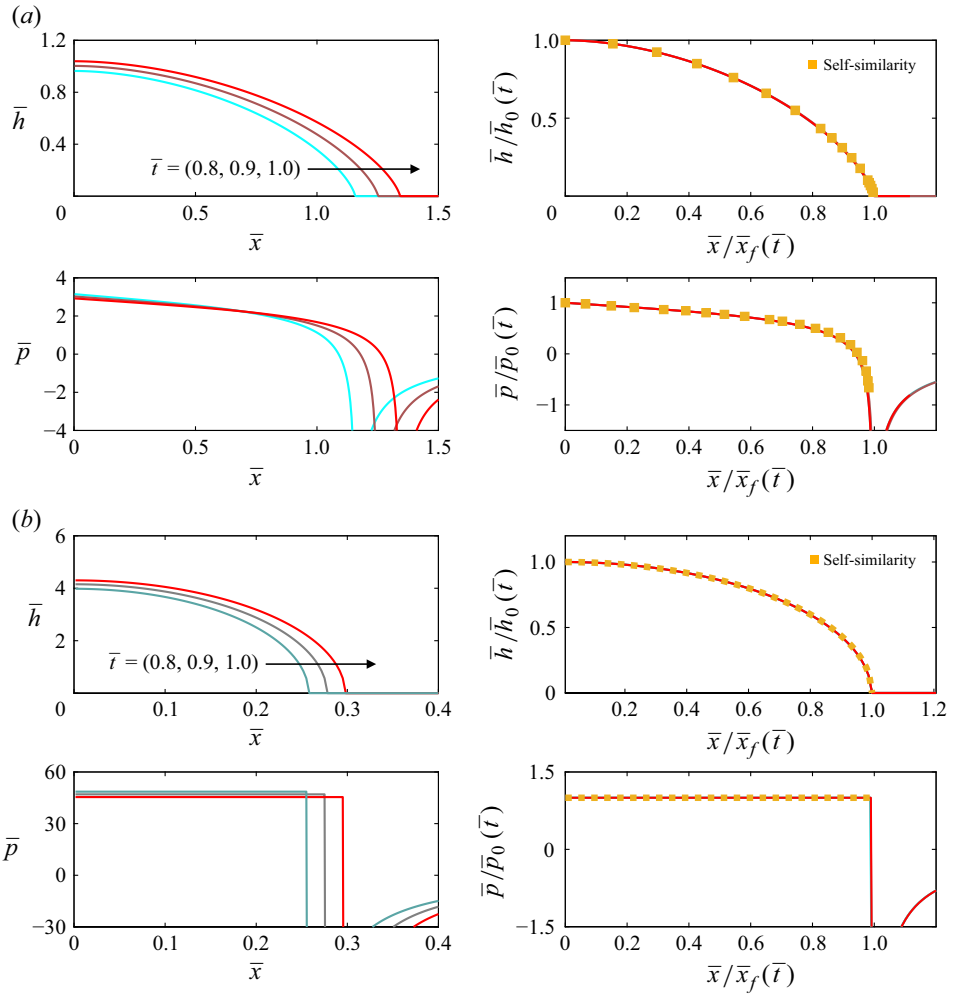


Figure 11. Comparison between the time-dependent numerical solutions and the self-similar solutions in terms of series solutions (Spence & Sharp 1985; Detournay 2004) for the standard situation of hydraulic fracturing using incompressible Newtonian fluids at constant injection rates: (*a*) $\Pi_k = 0$, and (*b*) $\Pi_k = 10$. Here, we focus on the profile shape and pressure evolution. In the numerical simulations, we have imposed $N = 300$ space grids on a domain of length $L_d = 1.5$ in (*a*), and $N = 150$ and $L_d = 0.5$ in (*b*).

condition $2^{-3/2}\, E(1-\sigma^2)^{-1}\, h(x_f - x)^{-1/2} = K_c$ as $x \to x_f^-$, which can also be written as $2\pi^{-1} x_f^{1/2} \int_0^{x_f} p(x_f^2 - x^2)^{-1/2}\, \mathrm{d}x = K_c$, we obtain $\bar{p}_m \sim 2^{-4/3}\pi^{4/3}\Pi_k^{4/3}\, \bar{t}^{-1/3}$ in the toughness-dominated regime, when pressure remains spatially uniform, $p = p_m$. A comparison is shown in figures 11(*b*) and 12(*b*) between the time-dependent numerical solutions and the asymptotic solutions at three different times, $\bar{t} = 0.8, 0.9, 1.0$ in the toughness-dominated regime with $\Pi_k = 10$. Here, we impose $N = 150$ space grids on a domain of length $L_d = 0.5$ in the numerical simulation. We have observed reasonable agreement at this space resolution in particular for the rescaled profile shapes and pressure fields in figure 11(*b*). The difference observed for the frontal prefactors in figure 12(*b*) is likely due to $\Pi_k = 10$ being not sufficiently large to perfectly approach the toughness-dominated regime, which predicts $\bar{x}_f \sim 0.32\, \bar{t}^{2/3}$, $\bar{h}_m \sim 4.0\, \bar{t}^{1/3}$ and $\bar{p}_m \sim$

https://doi.org/10.1017/jfm.2026.11619 Published online by Cambridge University Press

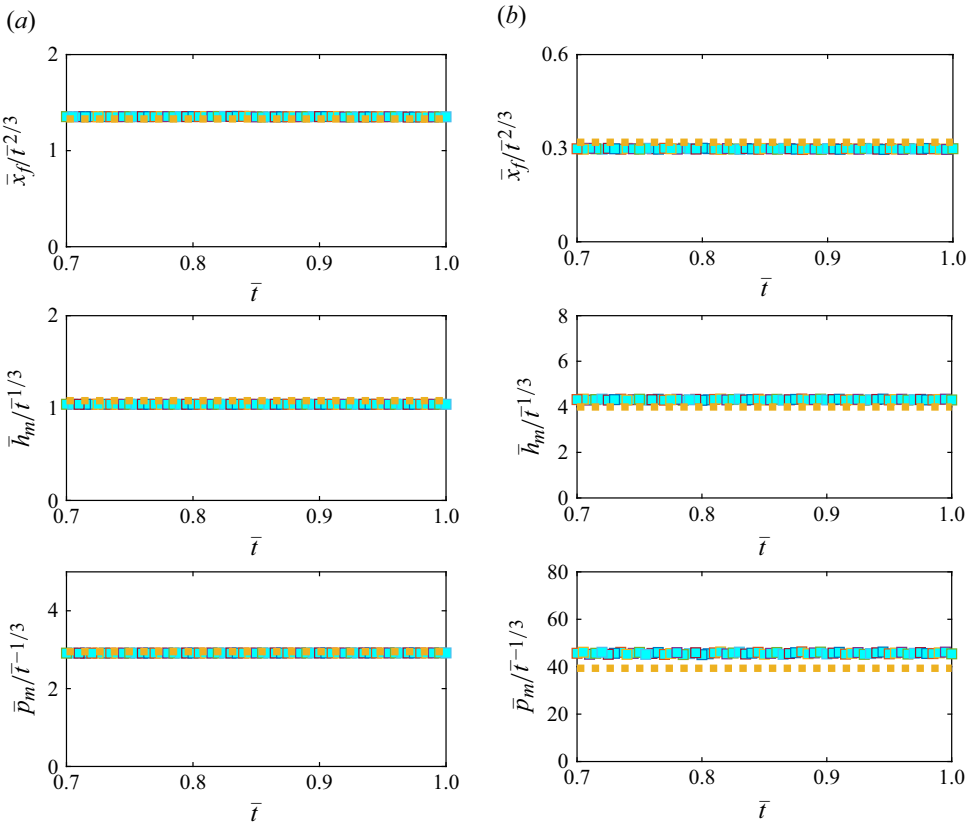


Figure 12. Comparison between the time-dependent numerical solutions and the self-similar solutions in terms of series solutions (Spence & Sharp 1985; Detournay 2004) for the standard situation of hydraulic fracturing using incompressible Newtonian fluids at constant injection rates: (*a*) $\Pi_k = 0$ when $\bar{x}_f \sim 1.33\,\bar{t}^{2/3}$, $\bar{h}_m \sim 1.08\,\bar{t}^{1/3}$ and $\bar{p}_m \sim 2.95\,\bar{t}^{-1/3}$ based on the viscosity-dominated self-similar solutions; and (*b*) $\Pi_k = 10$ when $\bar{x}_f \sim 0.32\,\bar{t}^{2/3}$, $\bar{h}_m \sim 4.0\,\bar{t}^{1/3}$ and $\bar{p}_m \sim 39\,\bar{t}^{-1/3}$ based on the toughness-dominated self-similar solutions. Here, we focus on the frontal laws. The orange lines correspond to the self-similar solutions, while the symbols correspond to the numerical solutions of the original time-dependent system. In the numerical simulations, we have imposed $N = 300$ space grids on a domain of length $L_d = 1.5$ in (*a*), and $N = 150$ and $L_d = 0.5$ in (*b*).

$39\,\bar{t}^{-1/3}$. Otherwise, there could also be some influence of low grid resolution as well as unfinished time transition.

Overall, we consider that the scheme is able to capture both the profile shape and the pressure evolutions during hydraulic fracturing of elastic solids in both the viscosity-dominated and toughness-dominated regimes. This is particularly true for the profile shape solutions. In the example calculations, numerical error first starts to appear for the pressure solutions approaching the location of pressure singularity, and more space grids are needed if the particular interest is to investigate the structure of the pressure singularity approaching the tip.

We expect similar behaviours for the numerical scheme presented in this appendix for foam-driven fracturing, when we further integrate the influence of foam compressibility and plug flow rheology in the nonlinear differential–integral system. We have tried to use a simple/clean scheme that is able to provide the physical insights of interest. But we also note that other numerical techniques may be used to better resolve the pressure singularity near the tip, such as the mesh concentration techniques in a moving domain.

https://doi.org/10.1017/jfm.2026.11619 Published online by Cambridge University Press

An alternative treatment is simply to integrate the asymptotic solutions to resolve the tip structure. An interested reader can refer to more specific publications on this topic (e.g. Peirce & Detournay 2008; Detournay 2016; Donsov 2017; Liu, Lecampion & Garagash 2019; Zia & Lecampion 2020).

Appendix B. The $\tau_w \propto Ca^{1/2}$ and $\tau_w \propto Ca^{2/3}$ behaviours

We briefly comment on the leading-order physics behind the $\tau_w \propto Ca^{1/2}$ behaviour for the plug flow of foam and the $\tau_w \propto Ca^{2/3}$ behaviour for standard capillary film flows. In both cases, the capillary number is defined as $Ca \equiv \mu\,|u|/\gamma$, where $|u|$ is the velocity scale in the primary flow direction, and the wall shear stress is given by $\tau_w = \mu\,\partial u/\partial z|_{z=0}$, by definition, but its value depends on the thickness scale of the viscous thin film. The central part is to obtain an estimate of the film thickness in different flow conditions when the influence of wetting and capillary forces is dominant.

For the plug flow of foam, the focus of the present work, i.e. the wall shear stress, can be estimated by $\tau_w \approx \mu\,|u|/h_0$, where h_0 is the thickness scale of the fluid film between the wall and a gas bubble (of radius $r \gg h_0$). The pressure (difference) scale that drives the thin film flow is estimated by $p_d \approx \mu\,|u|\,r/h_0^2$, which must also balance the capillary pressure $p_c \approx \gamma/r$ (more specifically, for normal force balance; Denkov *et al.* 2006). Imposing $p_d \sim p_c$, we arrive at an estimate for the thickness of the viscous thin film $h_0/r \approx (\mu\,|u|/\gamma)^{1/2} = Ca^{1/2}$. We then obtain $\tau_w/(\gamma/r) \approx (\mu\,|u|/\gamma)^{1/2} = Ca^{1/2}$. This argument is consistent with the theory of e.g. Denkov *et al.* (2006).

For standard thin film flow driven by capillary forces in the long wave limit, the wall shear stress is also estimated by $\tau_w \approx \mu\,|u|/h_0$, and the pressure (difference) scale is also given by $p_d \approx \mu\,|u|\,r/h_0^2$. The major difference is that now the pressure gradient that drives the thin film flow is given by $\partial p/\partial x = -\gamma\,\partial^3 h/\partial x^3$, which leads to an estimate $p_d/x_0 \approx \gamma h_0/x_0^3$, where $x_0 \gg h_0$ is a characteristic length scale of the capillary film. It is easy to see that the thickness of the film must now satisfy $h_0/x_0 \approx (\mu\,|u|/\gamma)^{1/3} = Ca^{1/3}$. We hence obtain $\tau_w/(\gamma/x_0) \approx (\mu\,|u|/\gamma)^{2/3} = Ca^{2/3}$. This argument is consistent with the standard theory of capillary film flows (e.g. Bretherton 1961; Eggers & Fontelos 2009; Zheng *et al.* 2018).

Appendix C. The influence of material toughness

C.1. On the propagation of a foam-driven fracture

C.1.1. Integrating an additional propagation condition

When the elastic solid is also brittle, we must also impose a crack propagation condition, e.g. in the form of a propagation law given by

$$\frac{E}{2^{3/2}(1-\sigma^2)}\,\frac{h}{(x_f(t)-x)^{1/2}} = K_c \quad \text{as } x \to x_f(t)^-, \tag{C1}$$

where K_c is a material property typically named material toughness (e.g. Rice 1968; Lister 1990*b*; Detournay 2004). Physically, (C1) indicates that the stress intensity must be large enough to break the atomic/molecular bonds at the fracture's tip to allow propagation. Regarding foam-driven fracturing, the physics remains the same as in the standard situation of hydraulic fracturing using Newtonian fluids. We note that in this work, we have followed Lister (1990*b*), and the prefactor in the propagation condition is smaller by a factor $\pi^{1/2}$ from the one used in e.g. Detournay (2004) and Garagash (2006). To our understanding, this is due to a difference in the definition of the material toughness

https://doi.org/10.1017/jfm.2026.11619 Published online by Cambridge University Press

K_c: the definition of the material toughness K_c is smaller by a factor $\pi^{1/2}$ in Lister (1990*b*), compared with the K_c in Detournay (2004) and Garagash (2006).

It is of use to have an estimate on whether or not material toughness plays an important role during foam-driven fracturing. Within the framework of the present model, which assumes that the plug flow of foam is quasi-steady in the tube, we can rewrite (C1) into a dimensionless form as

$$\frac{\bar{h}}{(\bar{x}_f(\bar{t}) - \bar{x})^{1/2}} = \Pi_k, \quad \text{as} \quad \bar{x} \to \bar{x}_f(\bar{t})^-, \tag{C2}$$

where we have introduced a dimensionless material toughness

$$\Pi_k \equiv \frac{2^{3/2}\left(1-\sigma^2\right)K_c x_c^{1/2}}{E h_c} = \frac{2^{7/2}\pi^{1/2} L p_i^{3/2}\left(1-\sigma^2\right)^{3/2} K_c}{3\rho_i c^2 a^{3/2} E^{3/2}}. \tag{C3}$$

Physically, Π_k provides a comparison between the influence of bond breaking at the fracture's tip and the viscous resistance of the thin film flow within the fracture.

In the weakly compressible regime, we are able to obtain more analytical insights regarding the influence of the propagation condition (C2). In § 3.2, we arrived at the scaling laws $\bar{x} \propto \bar{t}^{5/9}$ and $\bar{h} \propto \bar{t}^{4/9}$ in the weakly compressible and viscosity-dominated regime when the inlet pressure remains approximately constant, which then indicates that we must ensure $\bar{h}/\bar{x}^{1/2} \propto \bar{t}^{1/6} \gg \Pi_k$, i.e. $\bar{t} \gg \Pi_k^6$, to self-consistently neglect the influence of material toughness and stay in the viscous regime. That said, the influence of material toughness would always decrease with time for foam-driven fracturing, compared with the influence of viscous resistance of the foam flow within the fracture. For sufficiently large times, we expect the predictions of the viscous regime as described in the main text to work well.

C.1.2. Representative numerical observations

In the code, the propagation condition (C2) can be integrated in the same way as in our previous treatment regarding the backflow dynamics following hydraulic fracturing (see e.g. Appendix A of Zheng 2025*a*). At each time step, we now include

$$\frac{h^i_{n_f-1}}{(x_{n_f} - x_{n_f-1})^{1/2}} = \Pi_k, \tag{C4}$$

to account for the influence of Π_k. When $\Pi_k > 0$, (C4) provides an additional resistance at each time step, and propagation is allowed only if $h^i_{n_f-1}$ is sufficiently large. If $h^i_{n_f-1}$ is not large enough, then the front n_f remains unchanged at the specific time step, and fluid injection leads to an increase in $h^i_{n_f-1}$. Note that with this scheme, for any given spatial and temporal resolution (Δx and Δt), there exists a threshold Π_k value below which numerical solutions are available. But if Π_k is too large, then the fracture is not able to initiate.

Representative numerical results are then provided in figure 13, where we have imposed $\{\Pi_c, \Pi_k\} = \{0.001, 0\}$ (the solid curves) and $\{\Pi_c, \Pi_k\} = \{0.001, 0.01\}$ (the dash-dotted curves). To highlight the influence of Π_k, the numerical solutions for the profile shape $\bar{h}(\bar{x}, \bar{t})$, elastic pressure $\bar{p}(\bar{x}, \bar{t})$ and foam density $\bar{\rho}(\bar{x}, \bar{t})$ are provided at the same target times $\bar{t} = 400, 450, 500$ as those in figure 2 (when $\{\Pi_c, \Pi_k\} = \{0.001, 0\}$ in the viscosity-dominated regime). We have observed in these numerical simulations that the influence of material toughness is obvious at these target times: when $\Pi_k = 0.01$, the fracture's length becomes shorter at the same target times due to the additional resistance of material

https://doi.org/10.1017/jfm.2026.11619 Published online by Cambridge University Press

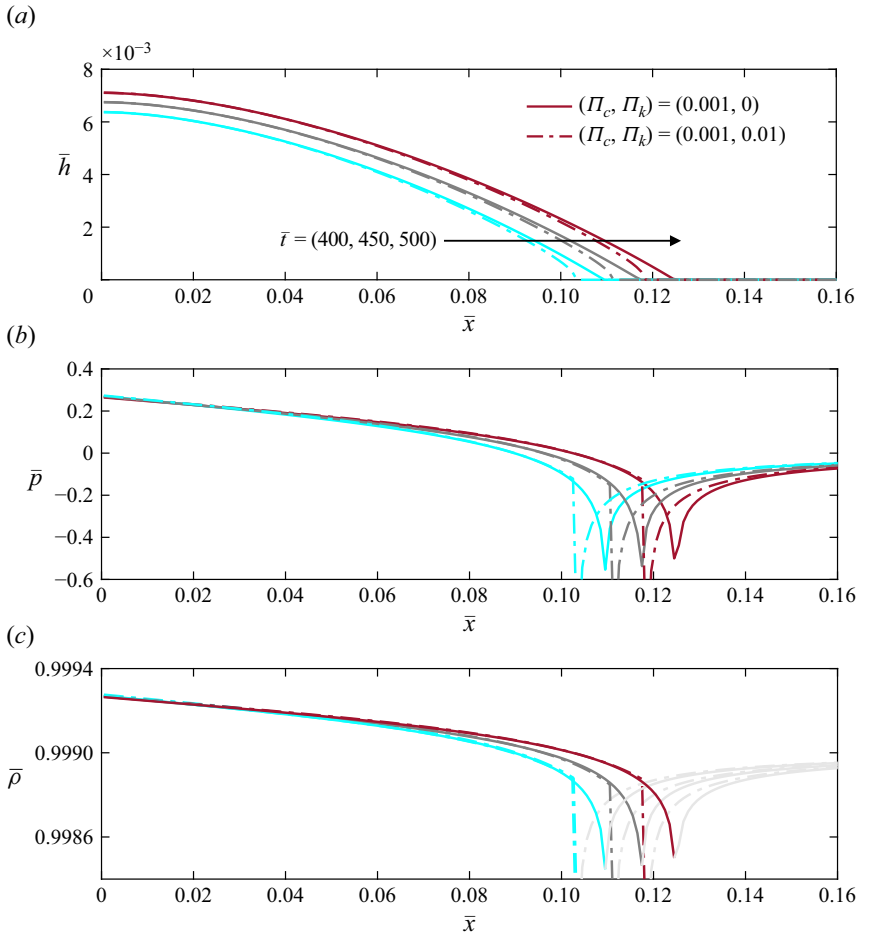


Figure 13. Representative numerical solutions of foam-driven fracturing at dimensionless times $\bar{t} = 400, 450, 500$ when we impose $\{\Pi_c, \Pi_k\} = \{0.001, 0\}$ (the solid curves) and $\{\Pi_c, \Pi_k\} = \{0.001, 0.01\}$ (the dash-dotted curves). We have imposed $N = 250$ space grids on a domain with $\bar{L}_d = 0.2$ in the simulations when $\Pi_k = 0.01$ for a sense of numerical error. The $\bar{p}(\bar{x}, \bar{t})$ values ahead of the front represent the normal elastic stress along the axis, while the $\bar{\rho}(\bar{x}, \bar{t})$ values ahead of the front contain no physical meaning because there exists no fluid. The density solutions ahead of the fracture's tip have no physical meaning and are marked with a different colour.

breaking at the tip. At these fairly large target times, solutions in the bulk region are already quite close to the viscous solutions, while in the tip region, the solutions are still significantly affected by the material toughness. Also, when $\Pi_k = 0.01$, the fracture's profile shape is closer to the elliptic asymptote in the quasi-steady toughness-dominated regime, and the pressure drop is less significant within the fracture compared with the viscous solutions.

To obtain more insights, we also rescale appropriately the $\bar{h}(\bar{x}, \bar{t})$ and $\bar{p}(\bar{x}, \bar{t})$ solutions included in figure 13 based on their maximum values. The results are shown in figure 14. In the same figure, we also show self-similar solutions in several different regimes for a comparison, including those in the viscosity-dominated regime (those given in figures 6 and 10 when $\{\Pi_c, \Pi_k\} = \{0.001, 0\}$) and toughness-dominated regime (elliptic profile shape + constant pressure), and also the standard solutions of hydraulic fracturing with incompressible Newtonian fluids under constant injection rates (e.g. Spence & Sharp 1985;

https://doi.org/10.1017/jfm.2026.11619 Published online by Cambridge University Press

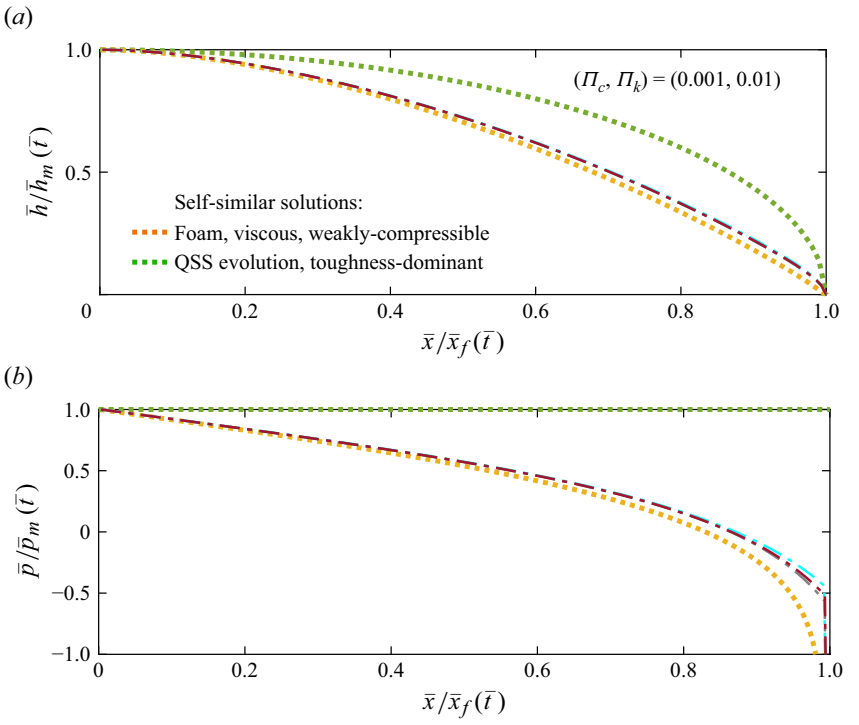


Figure 14. The appropriately rescaled numerical solutions of (*a*) $\bar{h}(\bar{x}, \bar{t})$ and (*b*) $\bar{p}(\bar{x}, \bar{t})$ based on their maximum values at dimensionless times $\bar{t} = 400, 450, 500$ when $\{\Pi_c, \Pi_k\} = \{0.001, 0.01\}$, as shown in figure 13. The self-similar solutions in both the viscosity-dominated regime (those in figure 6 when $\{\Pi_c, \Pi_k\} = \{0.001, 0\}$) and the toughness-dominated regime (elliptic profile shape + constant pressure) are also included for comparison. QSS indicates quasi-steady state.

Detournay 2004). The influence of material toughness is also clearly demonstrated, the physics of which is not significantly different from the standard situation of hydraulic fracturing with incompressible Newtonian fluids: as Π_k increases, the evolution gradually evolves in a quasi-steady fashion, when the influence of viscous flow becomes less important while the influence of material breaking at the fracture's tip becomes more dominant.

C.2. On the compression of foam in the injection tube

Observations made in the experiments of Lai *et al.* (2018) also indicate that foam compression could occur significantly in the injection tube before a fracture is initiated. This is also observed in the experiments of gas-driven fracturing in our own laboratory. Here, we provide brief comments on the influence of material toughness on this initial stage of foam compression in the tube. For a fracture to initiate, standard scaling analysis of (C1) indicates that $Eh_c/[(1-\sigma^2)a^{1/2}] \propto K_c$, where the length of an initial fracture is estimated by the radius of the tube a. The integral equation for pressure further indicates that $p_c \propto Eh_c/[(1-\sigma^2)a]$. We then arrive at an estimate of the pressure scale for fracture initiation:

$$p_c \propto K_c a^{-1/2}, \tag{C5}$$

https://doi.org/10.1017/jfm.2026.11619 Published online by Cambridge University Press

which indicates how much compression is needed in the injection tube before a fracture can be created in the elastic solid. This physical argument is no different from what has been discussed in Lai *et al.* (2018).

From the modelling point of view, to appropriately integrate the compression dynamics of foam flow in the injection tube, we are no longer allowed to impose the quasi-steady assumption for the plug flow of foam. That said, the important assumption behind § 2.2 to determine the influx q no longer applies. Equally importantly, it is not entirely clear what kind of foam rheology should be employed at this initial stage of fully unsteady compressible flow in the tube. Furthermore, within a short period right after a fracture is initiated, inertial effects may also become relevant at leading order, hence the Reynolds equation (2.7*a*) may also need to be appropriately modified. Detailed discussions may be of interest for a future work.

References

Balmforth, N.J. & Craster, R.V. 1999 A consistent thin-layer theory for Bingham plastics. *J. Non-Newtonian Fluid Mech.* **84**, 65–81.

Bessmertnykh, A.O. & Dontsov, E.V. 2019 A semi-infinite hydraulic fracture driven by a Herschel–Bulkley fluid. *J. Appl. Mech.* **86**, 121008.

Bickle, M., Goodman, D., Mair, R., Roberts, J., Selley, R., Shipton, Z., Thomas, H. & Younger, P. 2012 *Shale Gas Extraction in the UK: A Review of Hydraulic Fracturing*. The Royal Society and The Royal Academy of Engineering.

Bretherton, F.P. 1961 The motion of long bubbles in tubes. *J. Fluid Mech.* **10**, 166–188.

Cueto-Felgueroso, L. & Juanes, R. 2013 Forecasting long-term gas production from shale. *Proc. Natl Acad. Sci. USA* **110**, 19660–19661.

Denkov, N.D., Subramanian, V., Gurovich, D. & Lips, A. 2005 Wall slip and viscous dissipation in sheared foam: effect of surface mobility. *Colloids Surf. A* **263**, 129–145.

Denkov, N.D., Tcholakova, S., Golemanov, K., Subramanian, V., Gurovich, D. & Lips, A. 2006 Foam-wall friction: effect of air volume fraction for tangentially immobile bubble surface. *Colloids Surf. A* **282**, 329–347.

Detournay, E. 2004 Propagation regimes of fluid-driven fractures in impermeable rocks. *Intl J. Geomech.* **4**, 1–11.

Detournay, E. 2016 Mechanics of hydraulic fractures. *Annu. Rev. Fluid Mech.* **48**, 311–339.

Donsov, E.V. 2017 An approximate solution for a plane strain hydraulic fracture that accounts for fracture toughness, fluid viscosity, and leak-off. *Intl J. Fract.* **205**, 221–237.

Dontsov, E.V. & Kresse, O. 2018 A semi-infinite hydraulic fracture with leak-off driven by a power-law fluid. *J. Fluid Mech.* **837**, 210–229.

Dontsov, E.V. & Peirce, A.P. 2017 A multiscale implicit level set algorithm (ILSA) to model hydraulic fracture propagation incorporating combined viscous, toughness, and leak-off asymptotics. *Comput. Meth. Appl. Mech. Engng* **313**, 53–84.

Eggers, J. & Fontelos, M.A. 2009 The role of self-similarity in singularities of partial differential equations. *Nonlinearity* **22**, 1–44.

Garagash, D.I. 2006 Propagation of a plane-strain hydraulic fracture with a fluid lag: early-time solution. *Intl J. Solids Struct.* **43**, 5811–5835.

Hewitt, I.J., Balmforth, N.J. & Bruyn, J.R.D. 2015 Elastic-plated gravity currents. *Eur. J. Appl. Maths* **26**, 1–31.

Hinton, E.M. & Woods, A.W. 2018 Buoyancy-driven flow in a confined aquifer with a vertical gradient of permeability. *J. Fluid Mech.* **848**, 411–429.

Lai, C.-Y., Rallabandi, B., Perazzo, A., Zheng, Z., Smiddy, S.E. & Stone, H.A. 2018 Foam-driven fracture. *Proc. Natl Acad. Sci. USA* **115**, 8082–8086.

Lai, C.-Y., Zheng, Z., Dressaire, E., Ramon, G.Z., Huppert, H.E. & Stone, H.A. 2016*a* Elastic relaxation of fluid-driven cracks and the resulting backflow. *Phys. Rev. Lett.* **117**, 268001.

Lai, C.-Y., Zheng, Z., Dressaire, E. & Stone, H.A. 2016*b* Fluid-driven cracks in an elastic matrix in the toughness-dominated limit. *Phil. Trans. R. Soc. A* **374**, 20150425.

Lai, C.-Y., Zheng, Z., Dressaire, E., Wexler, J.S. & Stone, H.A. 2015 Experimental study on penny-shaped fluid-driven cracks in an elastic matrix. *Proc. R. Soc. A* **471**, 20150255.

https://doi.org/10.1017/jfm.2026.11619 Published online by Cambridge University Press

LENOACH, B. 1995 The crack tip solution for hydraulic fracturing in a permeable solid. *J. Mech. Phys. Solids* **43**, 1025–1043.
LISTER, J.R. 1990*a* Buoyancy-driven fluid fracture: similarity solutions for the horizontal and vertical propagation of fluid-filled cracks. *J. Fluid Mech.* **217**, 213–239.
LISTER, J.R. 1990*b* Buoyancy-driven fluid fracture: the effects of material toughness and of low-viscosity precursors. *J. Fluid Mech.* **210**, 263–280.
LISTER, J.R. & KERR, R.C. 1991 Fluid-mechanical models of crack propagation and their application to magma transport in dykes. *J. Geophys. Res.* **96**, 10049–10077.
LISTER, J.R., PENG, G.G. & NEUFELD, J.A. 2013 Viscous control of peeling an elastic sheet by bending and pulling. *Phys. Rev. Lett.* **111**, 154501.
LIU, D., LECAMPION, B. & GARAGASH, D.I. 2019 Propagation of a fluid-driven fracture with fracture length dependent apparent toughness. *Engng Fract. Mech.* **220**, 106616.
O'KEEFFE, N.J., HUPPERT, H.E. & LINDEN, P.F. 2018*a* Experimental exploration of fluid-driven cracks in brittle hydrogels. *J. Fluid Mech.* **844**, 435–458.
O'KEEFFE, N.J. & LINDEN, P.F. 2017 Hydrogel as a medium for fluid-driven fracture study. *Exp. Mech.* **57**, 1483–1493.
O'KEEFFE, N.J., ZHENG, Z., HUPPERT, H.E. & LINDEN, P.F. 2018*b* Symmetric coalescence of two hydraulic fractures. *Proc. Natl Acad. Sci. USA* **115**, 10228–10232.
PATZEK, T.W., MALE, F. & MARDER, M. 2013 Gas production in the Barnett Shale obeys a simple scaling theory. *Proc. Natl Acad. Sci. USA* **110**, 19731–19736.
PEIRCE, A. 2025 The arrest and recession dynamics of a deflating rectangular hydraulic fracture in a permeable elastic medium. *J. Fluid Mech.* **1017**, A42.
PEIRCE, A.P. & DETOURNAY, E. 2008 An implicit level set method for modelling hydraulically driven fractures. *Comput. Meth. Appl. Engng* **197**, 2858–2885.
RALLABANDI, B., ZHENG, Z., WINTON, M. & STONE, H.A. 2017 Wind-driven formation of ice bridges in straits. *Phys. Rev. Lett.* **118**, 128701.
RICE, J.R. 1968 Mathematical analysis in the mechanics of fracture. In *Fracture: An Advanced Treatise* (ed. H. Liebowitz) , chap. 3. Academic Press.
SAVITSKI, A.A. & DETOURNAY, E. 2002 Propagation of a penny-shaped fluid-driven fracture in an impermeable rock: asymptotic solutions. *Intl J. Solids Struct.* **39**, 6311–6337.
SCHULTZ, R., ATKINSON, G., EATON, D.W., GU, Y.J. & KAO, H. 2018 Hydraulic fracturing volume is associated with induced earthquake productivity in the Duvernay play. *Science* **359**, 304–308.
SPENCE, D.A. & SHARP, P. 1985 Self-similar solutions for elastohydrodynamic cavity flow. *Proc. R. Soc. A* **400**, 289–313.
SPENCE, D.A., SHARP, P.W. & TURCOTTE, D.L. 1987 Buoyancy-driven crack propagation: a mechanism for magma migration. *J. Fluid Mech.* **174**, 135–153.
TANIKELLA, S.S. & DRESSAIRE, E. 2022 Axisymmetric displacement flows in fluid-driven fractures. *J. Fluid Mech.* **953**, A36.
TAYLOR-WEST, J.J. & HOGG, A.J. 2021 The converging flow of viscoplastic fluid in a wedge or cone. *J. Fluid Mech.* **915**, A69.
WANG, D., CHEN, M., JIN, Y. & BUNGER, A.P. 2018 Impact of fluid compressibility for plane strain hydraulic fractures. *Comput. Geotech.* **97**, 20–26.
WARBURTON, K.L.P., HEWITT, D.R. & NEUFELD, J.A. 2020 Tidal grounding-line migration modulated by subglacial hydrology. *Geophys. Res. Lett.* **47**, e2020GL089088.
ZHENG, Z. 2024 Hydraulic fractures of the cusp shape in a Hele-Shaw cell. *J. Fluid Mech.* **995**, A17.
ZHENG, Z. 2025*a* The deflation of a hydraulic fracture subject to fluid withdrawal through a narrow conduit: the influence of material toughness. *J. Fluid Mech.* **1007**, A71.
ZHENG, Z. 2025*b* Hydraulic fractures of the dipole type subject to fluid withdrawal through a conduit. *J. Fluid Mech.* **1007**, A44.
ZHENG, Z., FONTELOS, M.A., SHIN, S., DALLASTON, M.C., TSELUIKO, D., KALLIADASIS, S. & STONE, H.A. 2018 Healing capillary films. *J. Fluid Mech.* **838**, 404–434.
ZHENG, Z., GUO, B., CHRISTOV, I.C., CELIA, M.A. & STONE, H.A. 2015 Flow regimes for fluid injection into a confined porous medium. *J. Fluid Mech.* **767**, 881–909.
ZHENG, Z. & NEUFELD, J.A. 2019 Self-similar dynamics of two-phase flows injected into a confined porous layer. *J. Fluid Mech.* **877**, 882–921.
ZIA, H. & LECAMPION, B. 2020 PyFrac: a planar 3D hydraulic fracture simulator. *Comput. Phys. Commun.* **255**, 107368.

https://doi.org/10.1017/jfm.2026.11619 Published online by Cambridge University Press